A MICROSTRUCTURAL STUDY OF THE EXTENSION-TO-SHEAR

FRACTURE TRANSITION IN CARRARA MARBLE

A Thesis

by

ERIKA RODRIGUEZ

Submitted to the Office of Graduate Studies of
Texas A&M University
in partial fulfillment of the requirements for the degree of

MASTER OF SCIENCE

August 2005

Major Subject: Geology

A MICROSTRUCTURAL STUDY OF THE EXTENSION-TO-SHEAR

FRACTURE TRANSITION IN CARRARA MARBLE

A Thesis

by

ERIKA RODRIGUEZ

Submitted to the Office of Graduate Studies of
Texas A&M University
in partial fulfillment of the requirements for the degree of

MASTER OF SCIENCE

Approved by:

Chair of Committee,	Judith S. Chester
Committee Members,	Frederick M. Chester
	Giovanna Biscontin
Head of Department	Richard Carlson

August 2005

Major Subject: Geology

ABSTRACT

A Microstructural Study of the Extension-to-Shear Fracture Transition

in Carrara Marble. (August 2005)

Erika Rodriguez, B.S., New Mexico Institute of Mining and Technology

Chair of Advisory Committee: Dr. Judith S. Chester

Triaxial extension experiments on Carrara Marble demonstrate that there is a continuous transition from extension to shear fracture on the basis of mechanical behavior, macroscopic fracture orientation and fracture morphology where hybrid fractures with extension and shear fracture characteristics are formed at the intermediate stress conditions. Extension fracture surfaces display discrete, highly reflective cleavage planes and shear fracture surfaces are covered with calcite gouge and display grooves and striations that are aligned parallel to slip. This study uses the fractured samples that were formed under triaxial extension experiments to characterize 1) microscopic surface features using scanning electron microscopy, 2) fracture surface morphology using laser profilometry, and 3) off-fracture damage using optical microscopy. These data are used to test the step-crack model of fracture development for the formation of hybrid fractures.

Spectral analysis of the profiles demonstrates that microscopic roughness decreases gradually across the extension-to-shear fracture transition in both the orientations parallel and perpendicular to slip. However, macroscopic roughness gradually increases then decreases across the transition in the direction parallel to slip. The greatest macroscopic roughness occurs at the transition from extension fractures to

tensile-hybrid fractures and is attributed to the presence of macroscopic steps in hybrid fractures surfaces. The treads of the steps in the hybrid fracture surfaces have characteristics of extension fracture surfaces and the risers have characteristics of shear fracture surfaces. The treads have a right-stepping left lateral geometry that is consistent with the step-crack model. Thin sections of hybrid fractures display systematically spaced, pinnate, microfractures that emanate from both sides of the macroscopic fracture surface. The pinnate fractures on both sides correlate across the macroscopic fracture, suggesting that they are precursory to the formation of the macroscopic fracture surface. The spacing to length ratio of the pinnate fractures and the macroscopic orientation of the fracture surface are also consistent the relationship dictated by the step-crack model of fault formation.

ACKNOWLEDGEMENTS

TABLE OF CONTENTS

LIST OF FIGURES

LIST OF TABLES

1. INTRODUCTION

Extension fracture and shear fracture are macroscopic modes of brittle failure that have long been recognized in rock deformation experiments [*Jaeger and Cook*, 1969]. An extension fracture is an opening mode crack (Mode I) that grows in plane under a tensile state of stress, where displacement is parallel to the minimum principal compressive stress, σ_3 (Fig. 1). Extension fractures are often considered analogous to joints in nature. A shear fracture is characterized by displacement parallel to the fracture surface and is formed under a compressive state of stress. Shear fractures are inclined to the maximum and minimum principal compressive stresses, often oriented at about 30° to σ_1 (Fig. 1). Shear fractures produced in the laboratory are used to model natural shear fractures (faults). For natural deformations, it has long been suggested that joints and shear fractures are end-members of a fracture continuum in which each fracture displays different degrees of opening and shear displacement [*Engelder*, 1999; *Hancock*, 1985]. In contrast, extension and shear fractures produced in the laboratory have been interpreted as distinctly different fracture types formed under specific states of stress [*Brace*, 1964; *Jaeger and Cook*, 1969].

Recently, *Ramsey and Chester* [2004] produced a continuous transition in macroscopic mode of failure from extension fracture to shear fracture in triaxial extension experiments with an increase in compressive stress (confining pressure). This transition in macroscopic mode of brittle failure is the first laboratory demonstrations of

_____

This thesis follows the style of *Journal of Geophysical Research*.
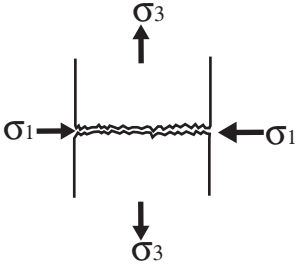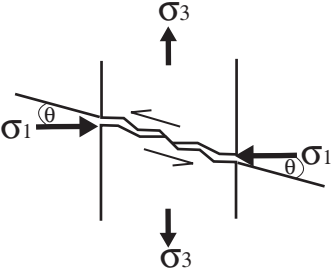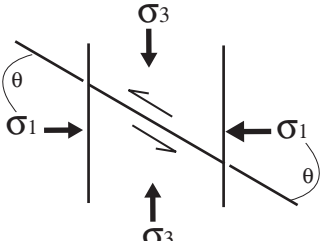
Figure 1. Schematic of the extension-to-shear fracture transition.

the formation of hybrid fractures, i.e., fractures that form under mixed tensile and compressive stress states, and at small angles to the maximum principal compressive stress. These new results suggest that a fracture continuum exists, and that models describing the formation of shear fractures also should be able to explain hybrid fracture (Fig. 1).

Although extension fracture can result from the in-plane propagation of a single microfracture, shear fractures are interpreted to form by the coalescence of en echelon microfractures that form within the process zone of a propagating fracture surface. In the stepped-crack model of *Reches and Lockner* [1994], the orientation of the macroscopic shear fracture is related to the spacing and length of the precursory, en echelon microfractures (Fig. 2). *Engelder* [1999] noted that natural fractures in the Mt. Desert Island granite that he interpreted as hybrid fractures also fit the stepped-crack relationship proposed by *Reches and Lockner* [1994]. This hypothesis can be tested using the experimental hybrid fractures produced by *Ramsey and Chester* [2004]. The continuous transition from extension to shear fracture documented in the triaxial extension experiments on Carrara marble could result from a systematic and progressive decrease in length and increase in spacing of precursory microfractures associated with increasing compressive stress states.

The objective of this paper is to characterize the detailed morphology and roughness of fracture surfaces, deformation mechanisms, and off-fracture damage of the samples from the study by *Ramsey and Chester* [2004] over the extension to shear fracture transition. These samples offer an unprecedented opportunity to investigate the

micromechanisms of fracture formation and to test the stepped-crack model for the development of hybrid shear fractures. The surface morphology is characterized using laser profilometry and scanning electron microscopy (SEM) and the associated damage is quantified using optical microscopy.
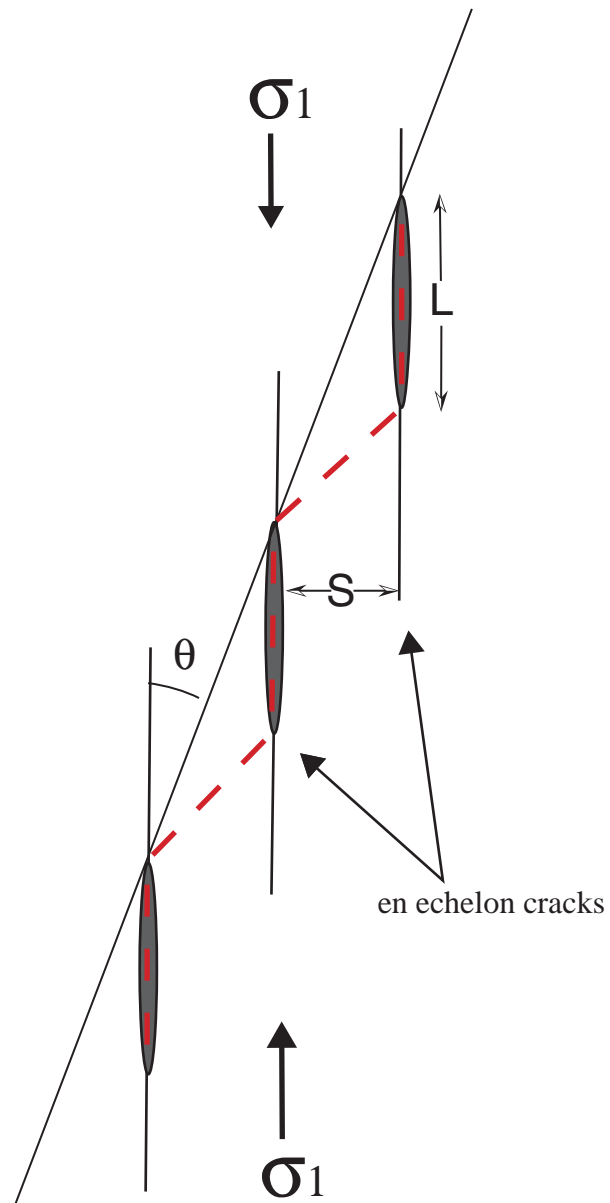
Figure 2. The step-crack model. *Reches and Lockner's* [1994] step-crack model predicts that cracks form in en echelon arrays by interaction with neighboring cracks, and that the macroscopic fracture orientation (θ) reflects the spacing (S) and length (L) of the en echelon cracks. *Engelder* [1999] proposes that this stepped-crack model can explain the formation of hybrid fractures with stepped-surface-geometries (red dashed lined) and fracture orientations

2. METHODS

Thirty-one dog-bone-shaped samples of Cararra marble were subjected to an axial extension at a rate of 2 X 10^{-2} mm s^{-1} under different compressive stress states [*Ramsey*, 2003; *Ramsey and Chester*, 2004]. The room temperature, triaxial experiments document a continuous transition from extension to shear fracture over confining pressures of 7.5 to 170 MPa. The transition is defined on the basis of the mechanical behavior, and the macroscopic orientation and surface morphology of the resultant fractures. The failure strength, fracture orientation, and fracture surface morphology at the macroscopic scale are reported in *Ramsey and Chester* [2004].

Carrara marble was selected for the experimental suite because it is nearly pure calcite and has less than 1% porosity. The calcite crystals are euhedral with triple point grain boundary intersections and they have a weak crystallographic preferred orientation (Fig. 3). The grain size ranges from 250-335μm. The undeformed marble has occasional thin mechanical twins and sporadic, intragranular, cleavage microfractures that are a few microns in length [*Fredrich et al.*, 1989; *Pieri et al.*, 2001].

After deformation, the surfaces of the extension fractures are oriented less than two degrees from σ_1 (Table 1) and they display discrete, highly reflective intragranular cleavage planes that produce a roughness at the grain scale [*Ramsey and Chester*, 2004]. The shear surfaces are covered with calcite gouge and display grooves and striations that are aligned with the maximum inclination of the surface. Some slip parallel to the macroscopic shear fracture occurred during the formation of each shear fracture before unloading (Table 1). The magnitude of the shear displacement is determined using a
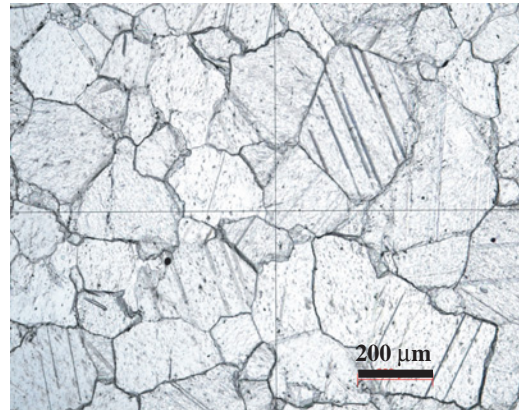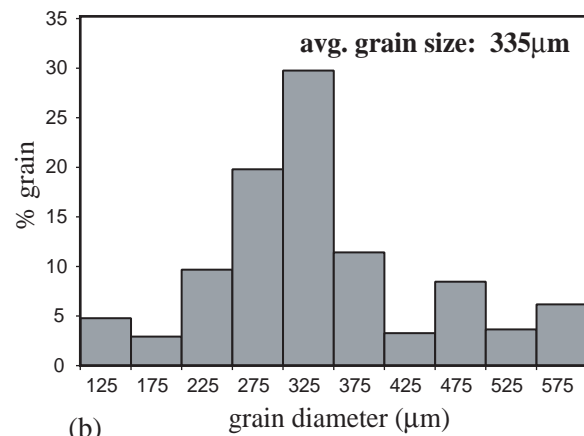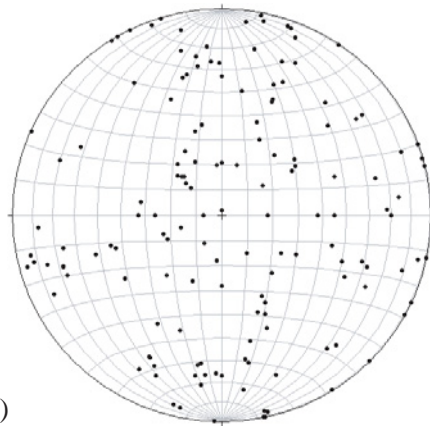
Figure 3. Undeformed Carrara marble. (a) Plane polarized light image of starting material showing ocassional twinning and triple junction grain boundary intersections. (b)Histogram of grain diameter showing a bin diameter of 50 μm. The average grain size determined was 335 μm. (c) Lower hemisphere, equal-area, stereographic projection, scatter plot displays no crystallographic preffered orientation.

Table 1. Data Set

Sample #	σ1 = P$_c$ (MPa)	σ3 (MPa)	Fracture Mode	*Fracture Angle	Slip (μm)	Method of Observation
4678	15	-9.6	Extension	1.8°	0	SEM
4641	15	-10.2	Extension	2.1°	0	LP, OM
4696	40	-11.4	Extension	2.1°	0	LP
4708	70	-15	T. Hybrid	3.7°	-	LP
4692	80	-12.9	T. Hybrid	5.4°	-	LP
4709	90	-13.8	T. Hybrid	6.1°	168	LP, OM
4688	100	-9.3	T. Hybrid	7.3°	-	LP, OM
4711	110	-9	C. Hybrid	11.1°	-	LP
4706	120	-9.1	C. Hybrid	12.4°	210	LP, OM
4643	130	-5.2	Shear	13.4°	-	LP
4705	140	-3.3	Shear	16.2°	-	LP, SEM
4687	150	-2.7	Shear	19.9°	-	LP
4693	170	6.5	Shear	21.6°	300	LP, OM

LP-laser profilometry, OM-optical microscopy, SEM-scanning electron microscopy
T. Hybrid = hybrid fracture formed under a tensile normal stress
C. Hybrid = hybrid fracture formed under a compressive normal stress
*fracture angle is the maximum angle between the fracture surface and the plane perpendicular to the sample axis

trigonometric relationship between the macroscopic fracture angle and the axial displacement recorded from the initiation of the major stress drop to the initiation of unloading. The macroscopic fracture angles of the shear fractures range from 13° to 22° to σ_1 (Table 1). The transitional surfaces, constituting the hybrid fractures, display characteristics of both the extension and shear surfaces, including highly reflective cleavage planes and patches of gouge. Similar to conditions for shear fracture, some nominal slip occurred along the macroscopic hybrid fracture surface under mixed stress state conditions before unloading (Table 1). Hybrid fracture surfaces are inclined 3°-12° from σ_1.

To document changes in surface morphology across the transition, the topography of the fracture surfaces of all samples was determined with a laser profilometer, and the fracture surfaces of two representative end-member samples were examined using the scanning electron microscope. For this, fracture surfaces were sputter-coated with ~4 nm of platinum palladium and examined in a LEO 1530 VP FE-SEM. To analyze the relationship between the microfractures and the macroscopic fracture surface, five representative samples across the transition were examined in thin section.

The roughness of each fracture surface was characterized using a profilometer consisting of a laser displacement sensor (Acuity, AR200-6) mounted on top of a linear shaft table that is advanced using a step motor. The laser displacement sensor operates by projecting a beam of visible laser light that creates a spot on the fracture surface. The angle of reflected light off the surface is detected by a line scan camera inside the sensor

head. The distance between the surface and the laser head is determined through a

triangulation computation. The best resolution (30 µm) is attained at the central part of

the vertical span (6.35mm) where the minimum spot size is 30 µm; the spot size at the

end points is 100 µm. The x-direction of the laser is monitored with a one-inch range

displacement transducer that is mounted horizontally on the linear shaft table. The y-

position is adjusted using a micrometer attached to the stage of the profilometer.

Samples were placed on the stage, manually tilted so that the fracture surface was

horizontal, and held in place by modeling clay. The laser displacement sensor was

positioned in the central area of the span to ensure the best resolution.

Ten traverses, spaced 4.45 mm apart, were made on each fracture surface, five

parallel and five perpendicular to the slip direction. Each traverse included a forward

and backward scan and an average of both profiles is presented in all cases. The power

spectral density for each wavelength was calculated following the procedures described

in *Bendat et al*. [1971].

After examining the surface of the fractures in representative samples, the two

halves of a fractured sample were mated and impregnated with epoxy. Petrographic

sections containing the fractured surface were prepared normal to the fracture surface

and in the direction parallel to slip. Maps documenting microfracture orientation,

distribution and density were made at a magnification of 20x. The maps of

representative extension and hybrid fractures record all microfractures observed. The

density of microfractures in the shear fracture samples is much greater, so shading is

used to indicate the variation in density based on measurements along four linear

traverses across the fracture. The microfracture orientations measured along the central traverse were plotted on a rose diagram. Twin thickness and density were measured for each thin section in order to calculate strain [*Groshong*, 1972] due to twinning for each fracture mode and the undeformed material. The measurements were made every half millimeter along a traverse that was perpendicular to the fracture surface and in the central part of the thin section. Twins were measured within a circular region half-millimeter in diameter.

3. RESULTS

3.1 Fracture Surface Descriptions

3.1.1 Extension Fracture

Some extension fracture surfaces display faint traces of gray mica swirls that vary in size and shape from being circular and about 5mm in diameter to long streaks that are a few millimeters wide and about 10 mm long. Most of the fracture surface is made up of variably oriented highly reflective calcite cleavage planes and grain boundary surfaces that are randomly oriented (Fig. 4). These fractures show no indication of shear striations or comminution along the surface.

The surface profiles document that all extension fractures are rough at all scales in the directions parallel (Fig.5a) and perpendicular (Fig. 5b) to maximum dip. The largest amplitude roughness elements are irregular in shape and orientation, and range up to 1mm in amplitude. No obvious correlation exists for these larger roughness elements from one profile to the next in an individual sample in either the slip-parallel or slip-perpendicular directions, consistent with an isotropic large-scale roughness character. The microscopic roughness (Fig. 6) displays amplitudes between 200-400 microns, which correspond to the average grain size of Carrara marble. Features the size of cleavage steps (Fig. 6) are also resolvable within the grain scale wavelets.

Individual calcite crystals often cleave along different planes to produce steps at a scale smaller than a single grain. In some instances the cleavage steps merge form a larger cleavage step. This characteristic is known as a river pattern and it is well
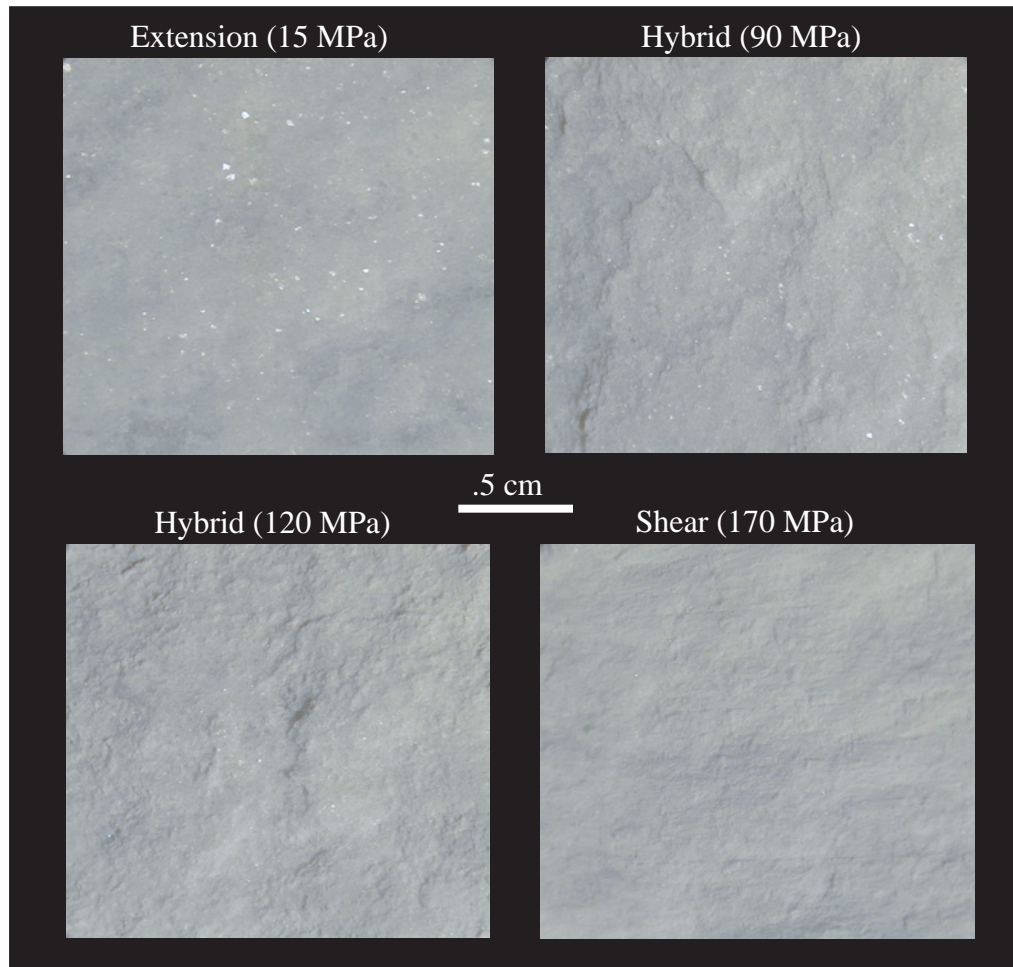
Figure 4. Photographs of macroscopic fracture surfaces. Extension fracture #4641 was formed at 15 MPa, tensile hybrid fracture #4709 was formed at 90 MPa, compressive hybrid fracture #4706 was formed at 120 MPa and shear fracture #4693 was formed at 170 MPa.
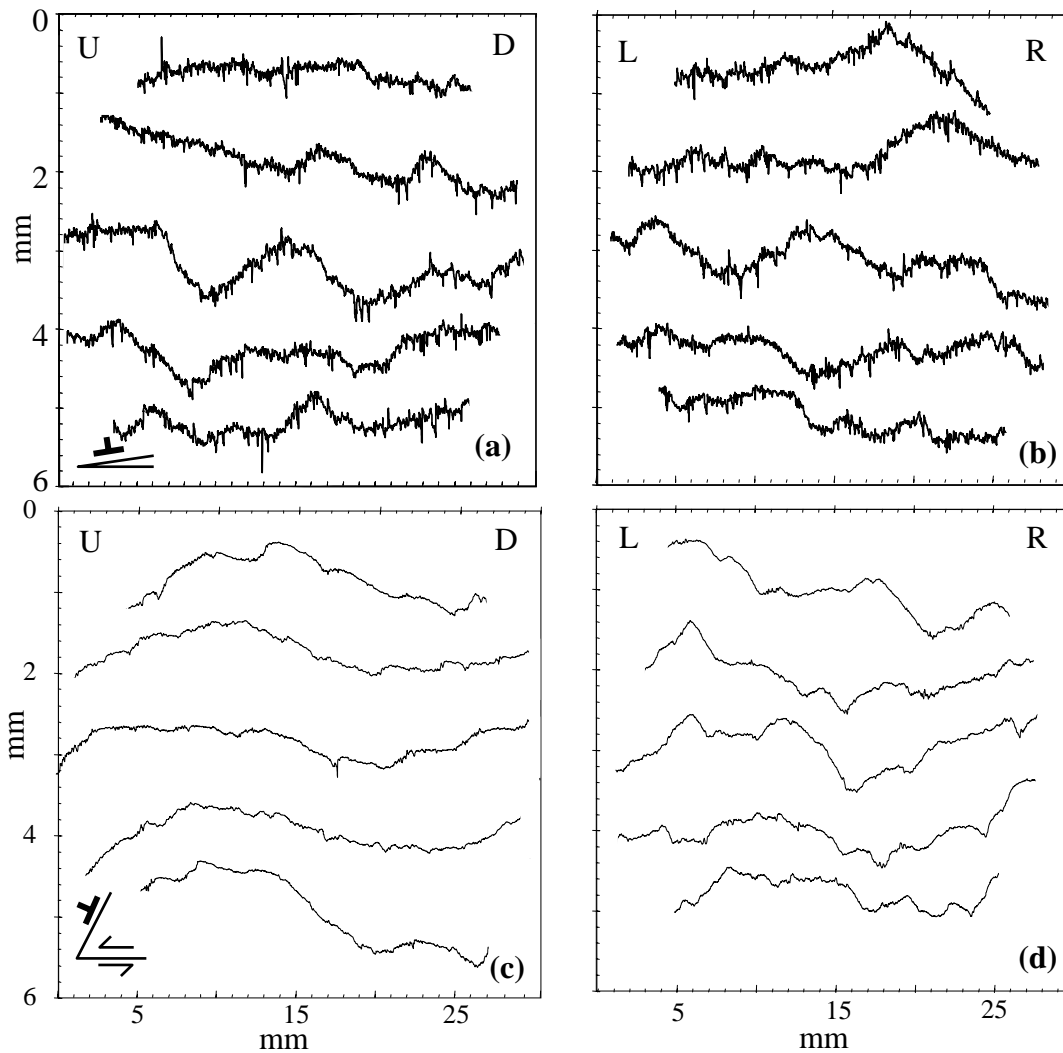
Figure 5. Representative profiles of the extension-to-shear fracture transition. Profiles of fracture surfaces measured displayed with a 5x vertical exaggeration. 'U' is up dip and 'D' is down dip; 'L' is left side of fracture surface and 'R' is right of fracture surface, with up dip side on top. (a) Extension fracture profile oriented parallel to the maximum dip direction (b) Extension fracture profile oriented perpendicular to the maximum dip direction. (c) Shear fracture profile oriented parallel to slip direction, (d) shear fracture profile oriented perpendicular to slip direction. Symbol on the bottom left hand corner of (a) and (c) displays the orientation of a plane perpendicular to the axis of the sample cylinder, arrows on (c) represent a left lateral sense of shear.
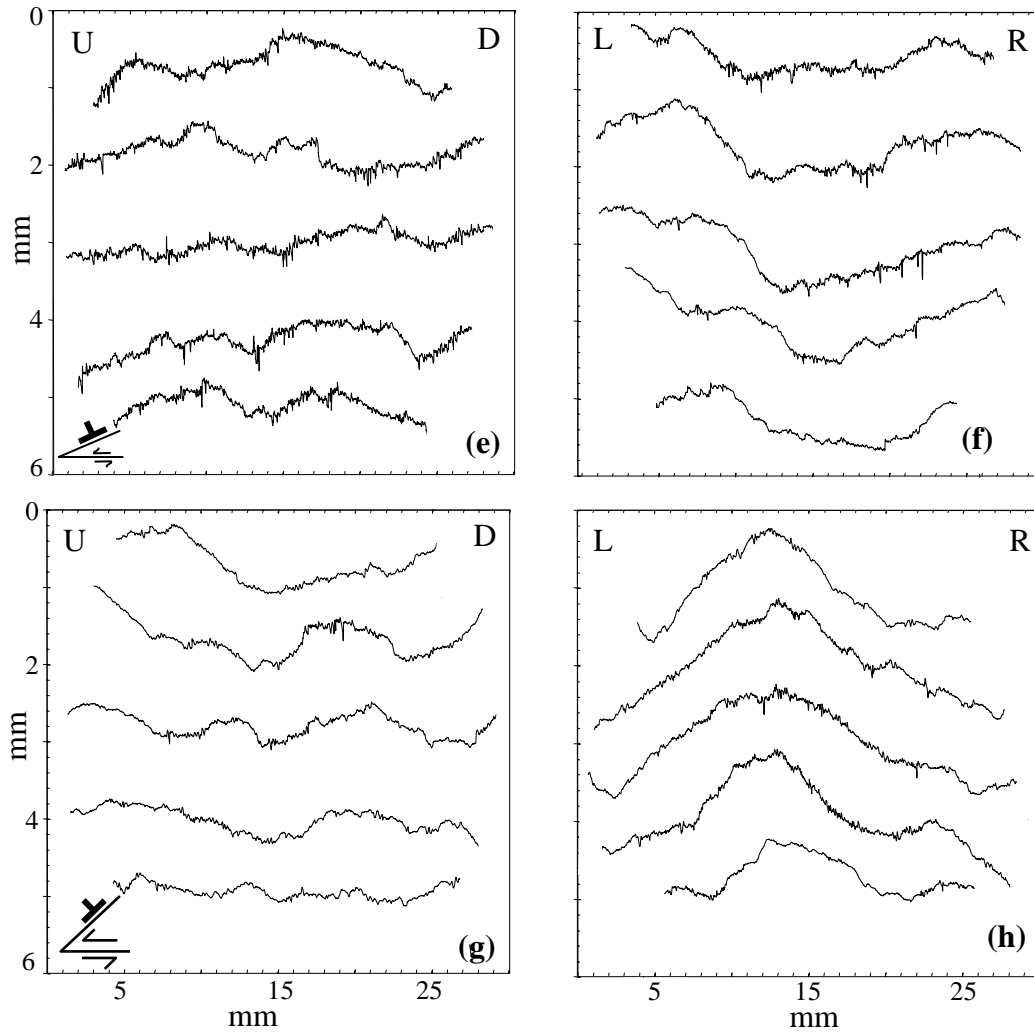
Figure 5 (cont.) (e) tensile hybrid fracture (90 MPa) profile oriented parallel to slip (f) tensile hybrid fracture profile oriented perpendicular to the maximum dip direction. (g) compressive hybrid fracture profile oriented parallel to slip, (h) compressive hybrid fracture profile oriented perpendicular to slip.
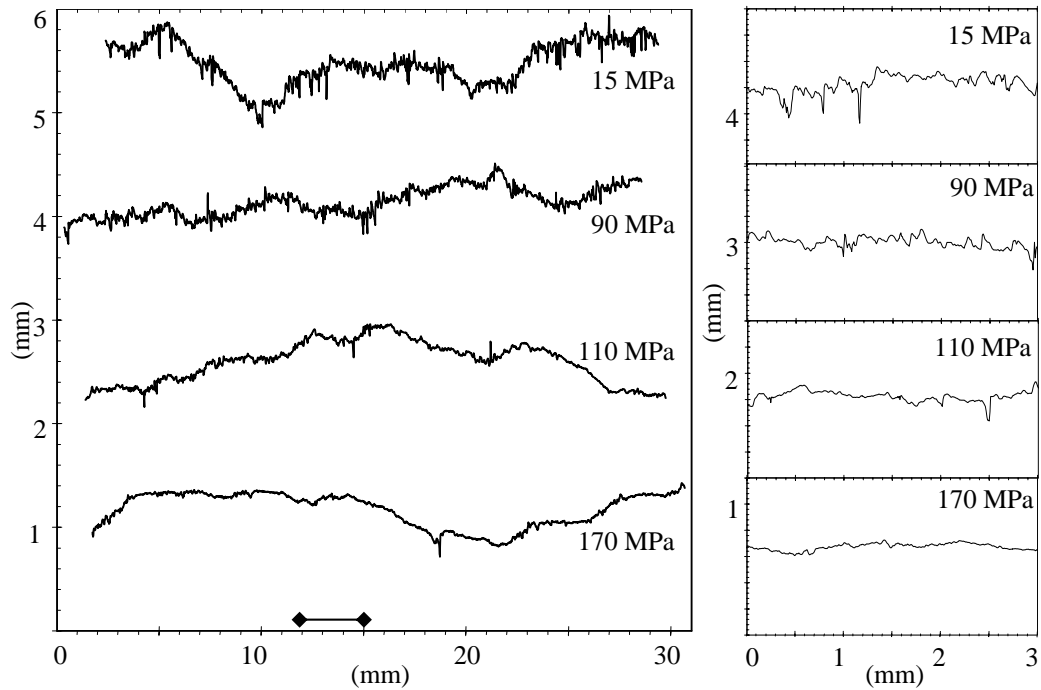
Figure 6. Profiles of microscopic roughness. Representative fracture surfaces of the extension to shear transition in the direction parallel to maximum dip or slip display the micro and macroscopic roughness. The location of the magnified profiles is marked on the horizontal axis of the macroscopic profiles. All profiles have 5X vertical exaggeration

recognized in materials where fracturing is dominated by cleavage [Fig. 7; *Friedel*, 1964; *Hull*, 1999; *Mardon et al.*, 1990]. The steps on a river pattern are aligned in the general direction of microfracture propagation. SEM images at different magnifications (Fig. 8) illustrate river patterns on an extension fracture surface at different scales. River patterns observed in localized regions of a single sample display a variety of microfracture propagation directions, including perpendicular and parallel to the maximum dip direction of the macroscopic fracture surface (Fig. 8).

3.1.2 Shear Fractures

Shear fracture surfaces are mostly covered with comminuted material and are striated; however, there are small areas where calcite cleavage planes are exposed (Fig. 4). The number and size of these regions gradually decrease as a function of confining pressure (Fig. 9). The shear fracture surfaces also have large corrugations that are oriented parallel to the slip direction. These corrugations are as long as the sample diameter and several millimeters in width. In most cases the corrugations are linear in the central part of the fracture surface; on the edges the corrugations are curved towards the outer part of the sample (Fig. 9). The length of the corrugations is much greater than the magnitude of slip on the fracture surface (Table 1).

The amplitudes of large-scale roughness elements on the shear fracture surfaces are similar to extension fractures in the direction perpendicular to slip, but are smaller for the direction parallel to slip (Fig. 5c). In the direction perpendicular to slip, features such as corrugations can be correlated between profiles (Fig. 5d). In the direction

parallel to slip, the three central profiles show the best correlation in shape (Fig. 5c). The outer two profiles are less similar since they traverse large grooves that curve out towards the edge of the sample. The microscale roughness of the shear fractures is similar for both the slip-parallel and slip-perpendicular directions; the wavelets have amplitudes of less than 50 microns (Fig.6).

The shear fracture surface deformed at 150 MPa displays comminuted particles a few microns in size and smaller (Fig. 10). Over ninety percent of the surface is covered by comminuted material. This observation can only be made qualitatively, since comminuted material was lost at the time of separating the two mates of the fracture. It is also likely that comminuted material was lost or dislodged during handling of the samples. Future experiments will address this problem. Areas not covered by comminuted material are made up of patches that are two or three grains in diameter. The exposed surfaces of these patches display river patterns on fractured surfaces and twins (Fig. 11). Localized river patterns (Fig. 11b) suggest that these patches propagated perpendicular to the slip direction of the macroscopic fracture shear surface. This would be consistent with Mode 3 growth of the macroscopic shear fracture. The steps of the river patterns observed on the shear fracture surface are smaller than those observed in the extension fracture regime at a similar magnification (compare Fig.8a and Fig.11b). SEM images of the shear fractures also illustrate that intragranular and grain boundary fractures formed.

Crack propagation direction
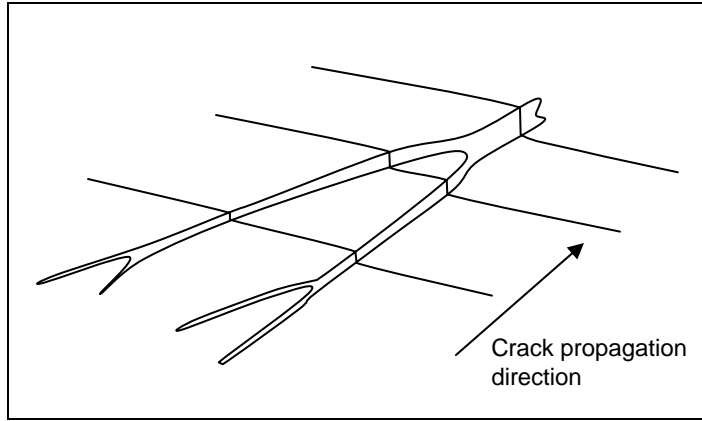
Figure 7. Schematic diagram of a river pattern.
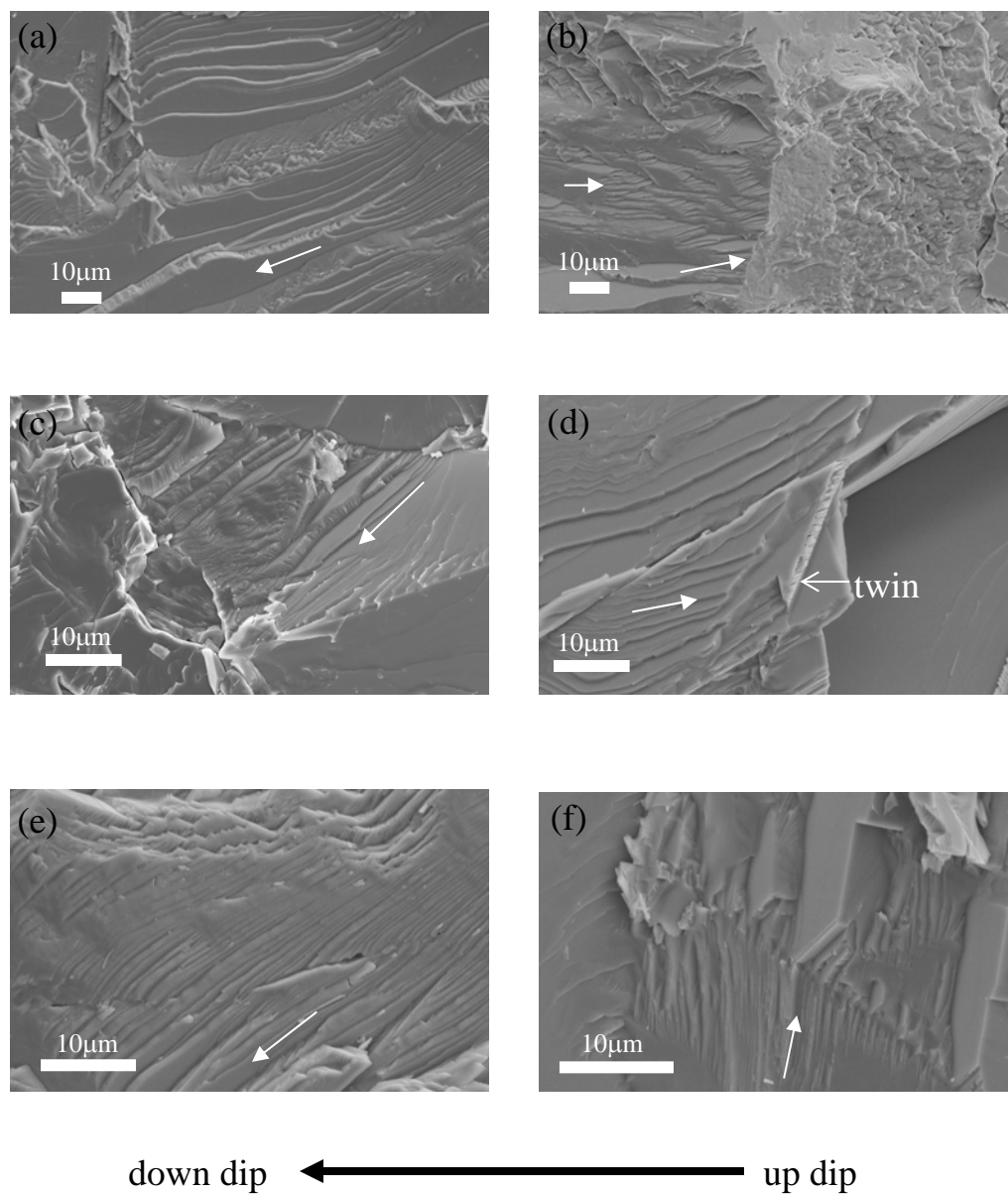
Figure 8. SEM images of an extension fracture (#4678, 15MPa). Examples of river patterns at different magnifications. White arrows indicate microcrack propagation direction, black arrow is parallel to the macroscopic dip direction which implies macroscopic fracture growth direction.
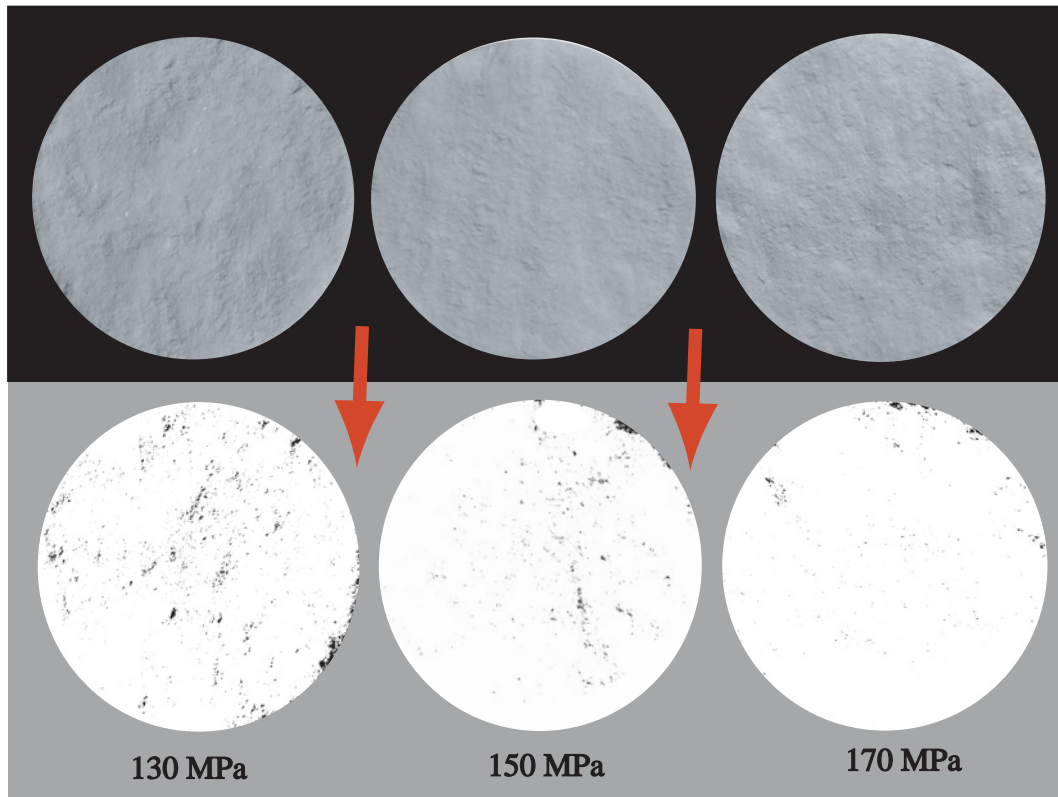
Figure 9. Threshold images of shear fractures surfaces. Top images are photographs of the fracture surfaces, bottom images are thresholed images deformed at 130, 150 and 170 MPa. Zones of comminution are displayed in white, and reflective calcite cleavage surfaces are displayed in black. Down dip direction is at the bottom of the fracture surface and arrows indicate slip orientation.
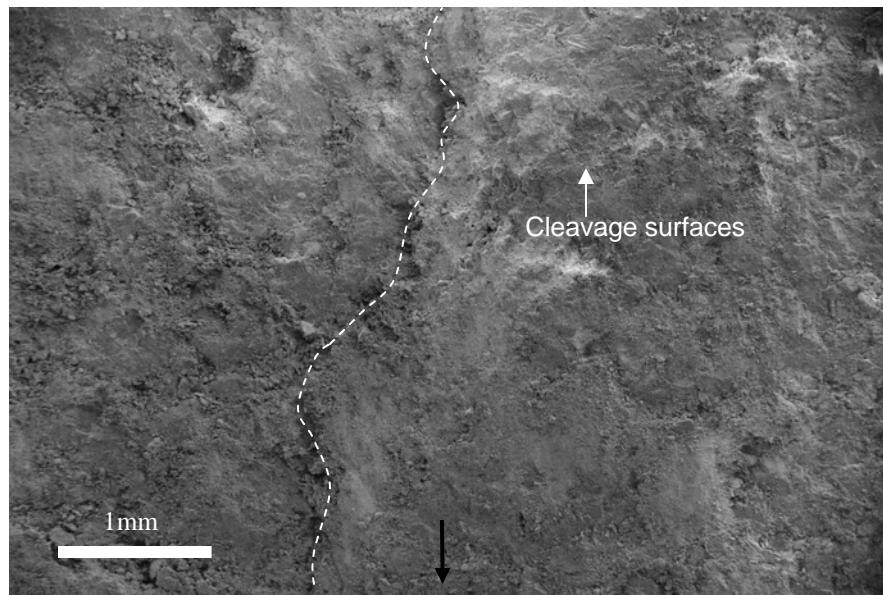
Figure 10. SEM image of a shear fracture surface at 20x magnification (#4705, 140 MPa). Black arrow indicates macroscopic slip direction, the dotted white curve outlines a macroscopic groove. A patch not covered by gouge exposes cleavage cracks.
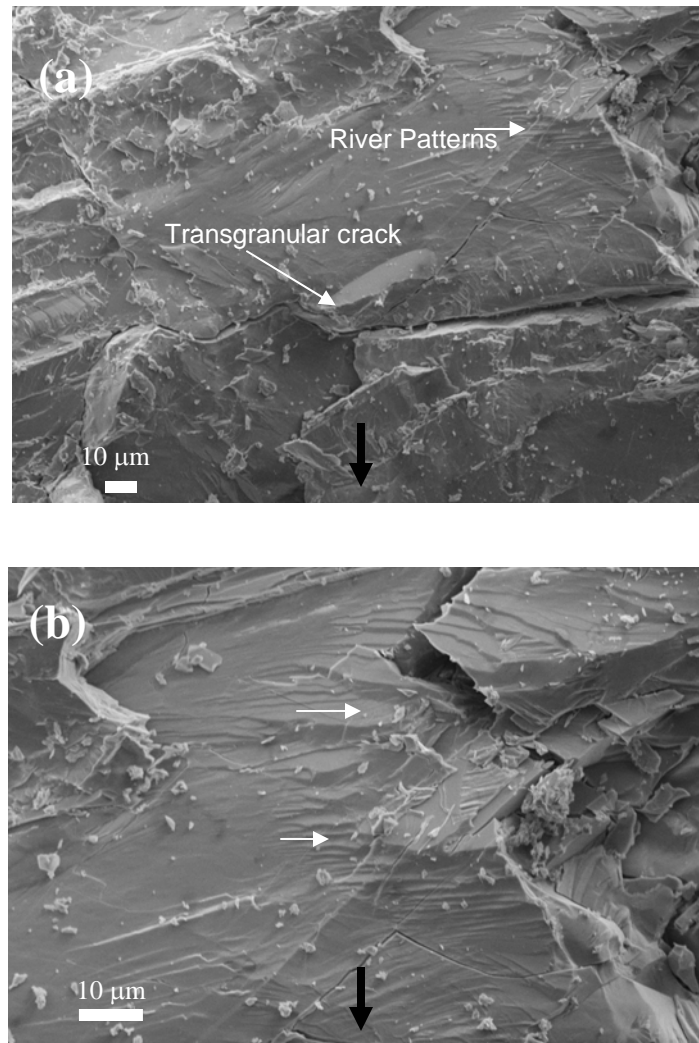
Figure 11. SEM images of a shear fracture surface (sample #4705, 140 MPa. The shear fracture surface displayed on this figure is a patch not covered by comminuted material, this allows us to see features such as river patterns (b) (compare the scale of these river patterns at 1000 times magnification) and the river patterns of an extension fracture at the same magnification (figures 3a&b). Also displayed in this photograph is an intergranular crack. White arrows indicate microcrack propagation direction, black arrow indicates macroscopic slip direction

3.1.3 Hybrid Fracture

At the macroscopic scale, hybrid fractures have characteristics of both extension

and shear surfaces (Fig. 4). The hybrids that form under tensile normal stress (70-100

MPa) are most similar to the extension fracture surfaces (i.e. surfaces are made up of

highly reflective cleaved calcite grains). Conversely, hybrids that form under a

compressive normal stress (110&120 MPa) are more similar to the shear fracture

surfaces in that they display comminution. The comminution typically occurs in

elongate bands that are generally oriented perpendicular to the macroscopic slip

direction. The percentage of the macroscopic fracture surface area that is covered by

comminuted material increases gradually from the tensile to the compressive hybrids

(Fig. 12).

The large scale roughness is greater in the slip-perpendicular direction than in

the slip-parallel direction. In the slip-parallel direction, large-scale amplitude features

are intermediate to extension and shear fracture surface roughness (Fig. 5e&g). In some

cases, large-scale amplitude features in the hybrids can be correlated across profiles in

the direction perpendicular to slip. The amplitudes of wavelets at the micro scale in both

slip- parallel and slip-perpendicular directions are intermediate compared to extension

and shear fractures. In addition, there is micro scale roughness variability along

individual traverses in both orientations; this is most evident in the profiles of the

hybrids formed under compressive normal stress (Fig. 5e-h & Fig. 13).

Profiles of the hybrids taken in the direction parallel to slip display the

segmented character of the fracture surface (Fig. 13). One segment type is preferentially

oriented nearly perpendicular to the core axis and is characterized by a rougher

microscopic character, similar to that displayed on the extension fracture surfaces.

These segments are arranged en echelon with a consistent step that is opposite to the

sense-of-shear (i.e. right-step for left-lateral-shear). The second type of segment is

oriented oblique to the core axis and displays a smoother microscopic roughness

character, similar to that of a shear fracture surface.

3.2 Off-fracture Deformation

3.2.1 *Extension Fracture*

In thin section, the extension fracture (Fig. 14) is a macroscopic fracture that is

composed of segments of microscopic cleavage planes and grain boundary

microfractures. A system of smaller intergranular and intragranular microfractures

emanate from the macroscopic fracture surface on both sides. The microfractures form

along cleavage planes and grain boundaries, range in length from 1 to 5mm, and are all

oriented approximately parallel to the macroscopic fracture surface (Fig.14). This

associated deformation occurs within half a millimeter of the macroscopic fracture

surface. Outside this zone of deformation only sporadic, intragranular, cleavage

microfractures and mechanical twins occur, consistent with that in the starting material.

The density of mechanical twins is constant across the deformation zone and is similar to

that of the staring material (Fig. 15).
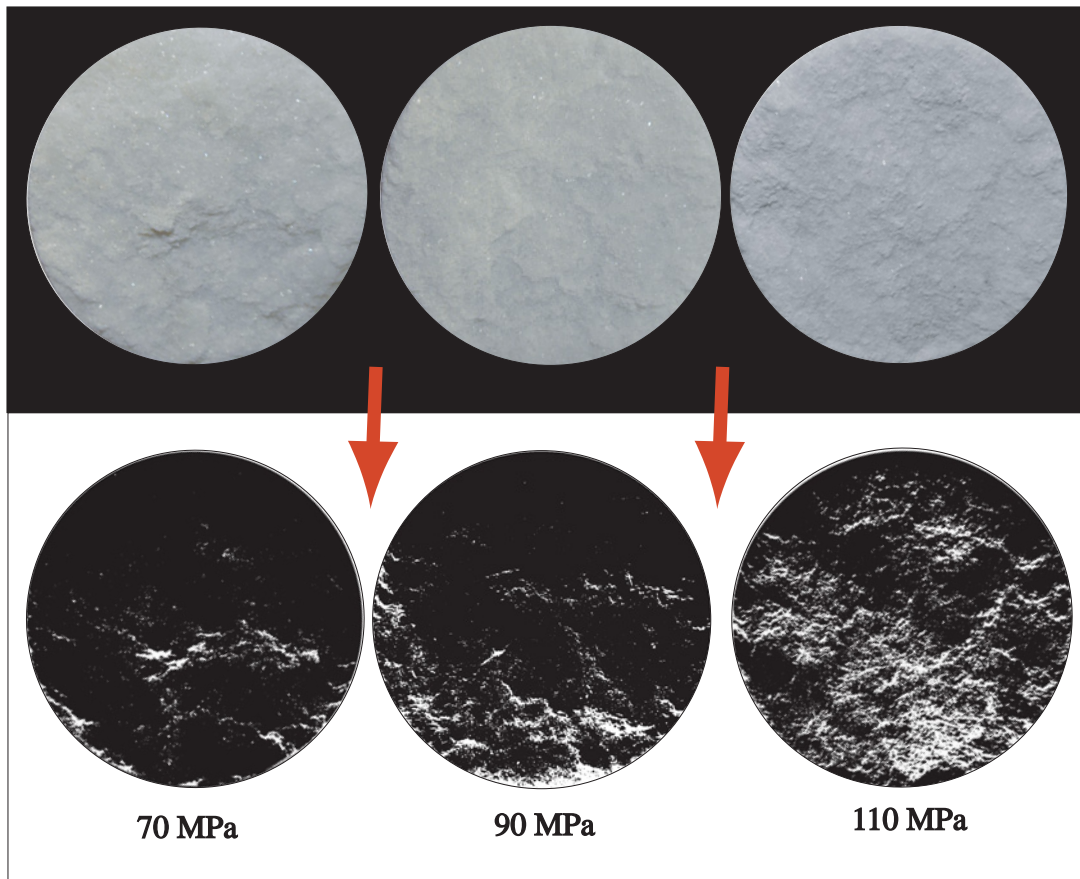
Figure 12. Threshold images of Hybrid fracture surfaces. Top images are photographs of fracture surfaces deformed at 70 MPa, 90 MPa and 110 MPa. The bottom images were thresholded using NIH software so that the comminuted zones would stand out. Comminuted zones are white pixels. Down-dip direction is at the bottom of the photograph for all cases, arrows indicate direction of dip.
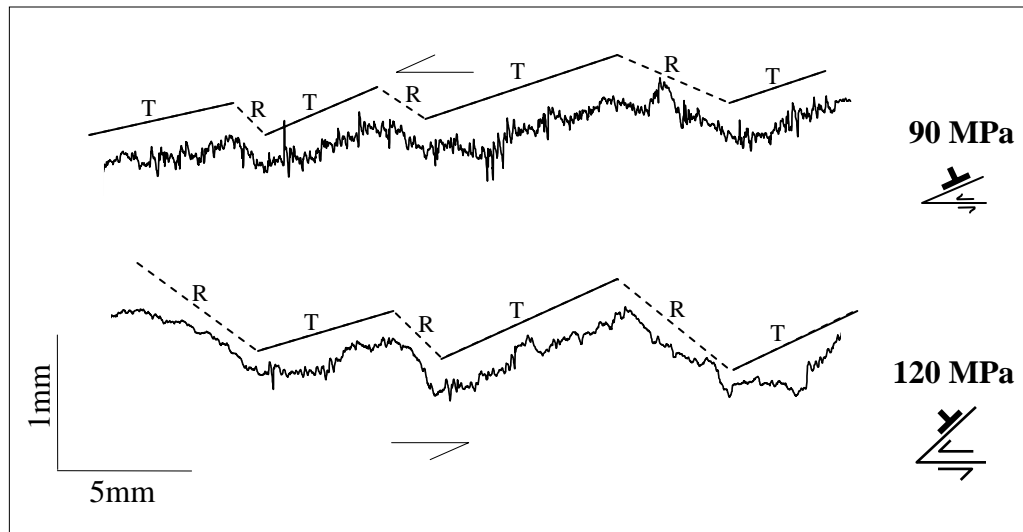
Figure 13. Profiles of hybrid fracture surfaces. Vertical exaggeration 5x. The profiles displayed are for hybrid samples deformed at 90 MPa and 120 MPa, The profiles display a macroscopic stepped geometry. The risers (R) are smoother and correspond to shear fracture surfaces; the treads (T) are rougher and correspond to extension surfaces, that are oriented in the direction perpendicular to the sample axis. The treads are right-stepping geometry with a left-lateral sense of shear.

3.2.2 Shear Fracture

The macroscopic shear fracture surface is bounded by a wide zone of deformation (Fig. 16). The macroscopic fracture surface in this sample is more planar than that those produced at lower confining pressures (Fig.14 & Fig. 16). It appears that a large fraction of comminuted material was displaced during the epoxy impregnation process and can be seen floating in the blue epoxy between the fracture surfaces. However some comminuted material still remains on the fracture surface inside small depressions that are less than one grain deep. Segments along the surface that display comminuted material also mark the locations where bounding grains contain up to three sets of twins. This high density twinning gives the grains a dark to black appearance (Fig. 16b). There are also darkened grains that are not covered by comminution.

A set of large subsidiary fractures that are oriented at approximately 20° from the macroscopic fracture surface (Fig. 16) are present on the shear fracture sample. These subsidiary fractures occur on both sides of the macroscopic fracture surface and extend from the central part of the fracture towards the outer edge of the sample (Fig. 16). Side 'A' of sample displays five right-stepping segments, four segments are between 4-5 mm in length and one is 1.5 mm long. On side 'B', there are 3 right-stepping segments; the larger is 4 mm in length and the two smaller ones are 2 mm long. The subsidiary fractures are open and in some cases display comminuted particles and a left-lateral sense of shear.

Microfracture density and twinning also increase around the macroscopic fracture surface and the subsidiary fractures (Fig. 15 & Fig. 16). There is a strong

microfracture fabric (Fig. 17) in which most microfractures are nearly parallel to the

maximum principal stress; there is about a 5° fluctuation in orientation above and below

the mean microfracture orientation. The highest fluctuation in orientation is associated

with the subsidiary fractures (Fig. 15c).

A second type of subsidiary fracture is located about five millimeters away from

the macroscopic fracture surface (Fig. 16). This large transgranular microfracture is

almost two centimeters in length and is nearly parallel to the maximum principal stress.

This fracture sharply follows grain boundaries and cleavage planes and there is little

microfracturing or twining associated with it; it is similar to an extension fracture. This

fracture could have formed at a lower confining pressure during the unloading portion of

the experiment.

3.2.3 Hybrid Fracture

The number of twins and microfractures varies along the macroscopic fracture

surface of the tensional and compressive hybrid fractures deformed at 90MPa and 120

MPa confining pressure, respectively (Fig. 18 & Fig. 19). The regions on the surface

that display the greatest number of microfractures and twinning are associated with

comminuted material and are located on the segments of the surface which are oriented

at a high angle to σ_1; these regions are more frequent in the compressive hybrid fractures.

There also is a set of microscopic fractures that extend away from the macroscopic

fracture surface. These fractures display a distinctive decrease in aperture with distance
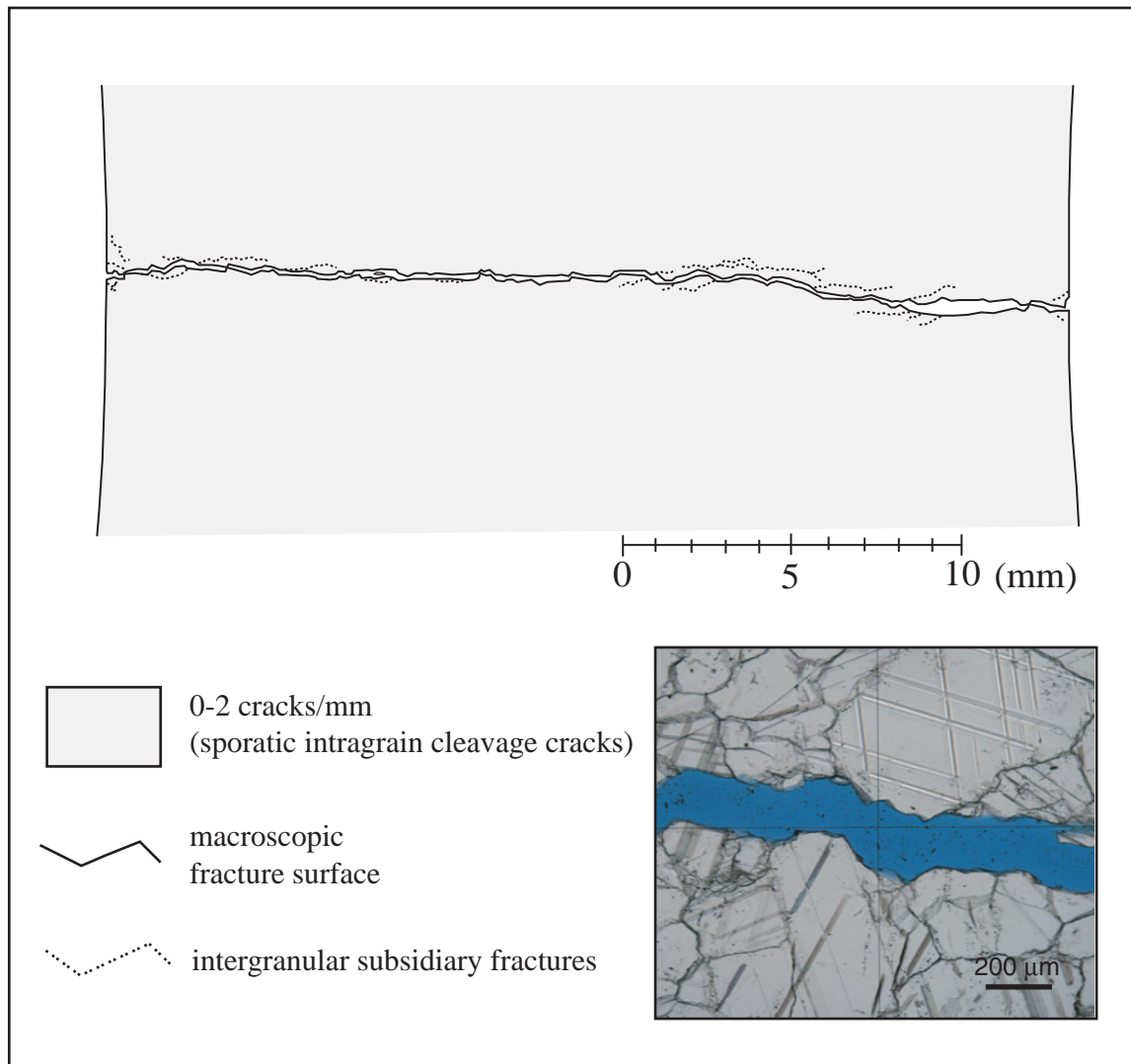
Figure 14. Microfracture map of extension fracture (sample #4641, 15 MPa).
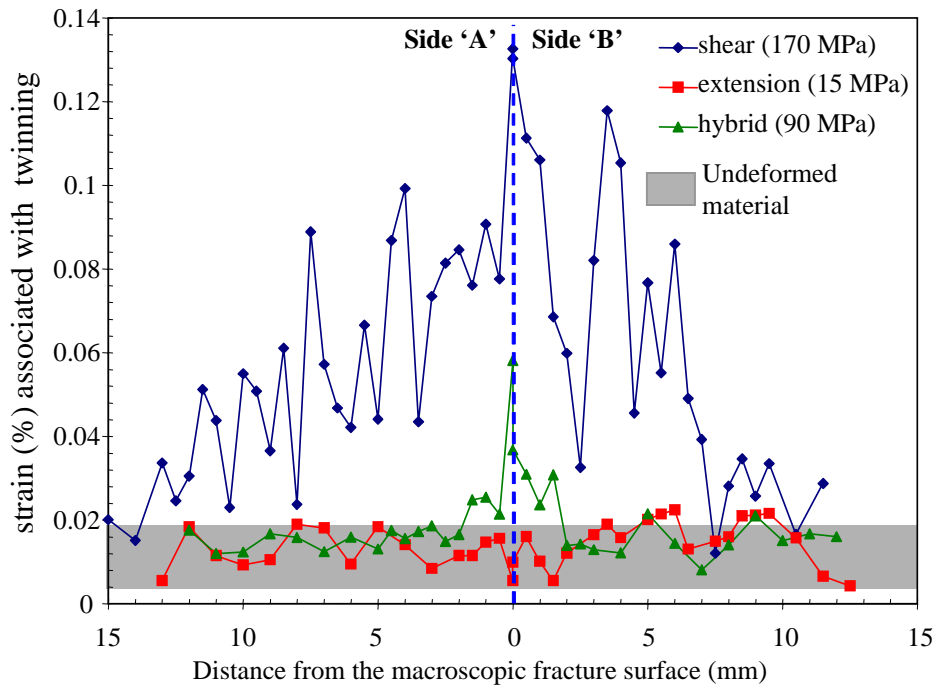
Figure 15. Plot of strain (%) due to twinning vs. distance. The strain (%) is plotted as a function of distance from the macroscopic fracture surface for an extension fracture, a shear fracture and a hybrid fracture. The strain due to twinning was also determined for the undeformed material and the range is shaded on the plot
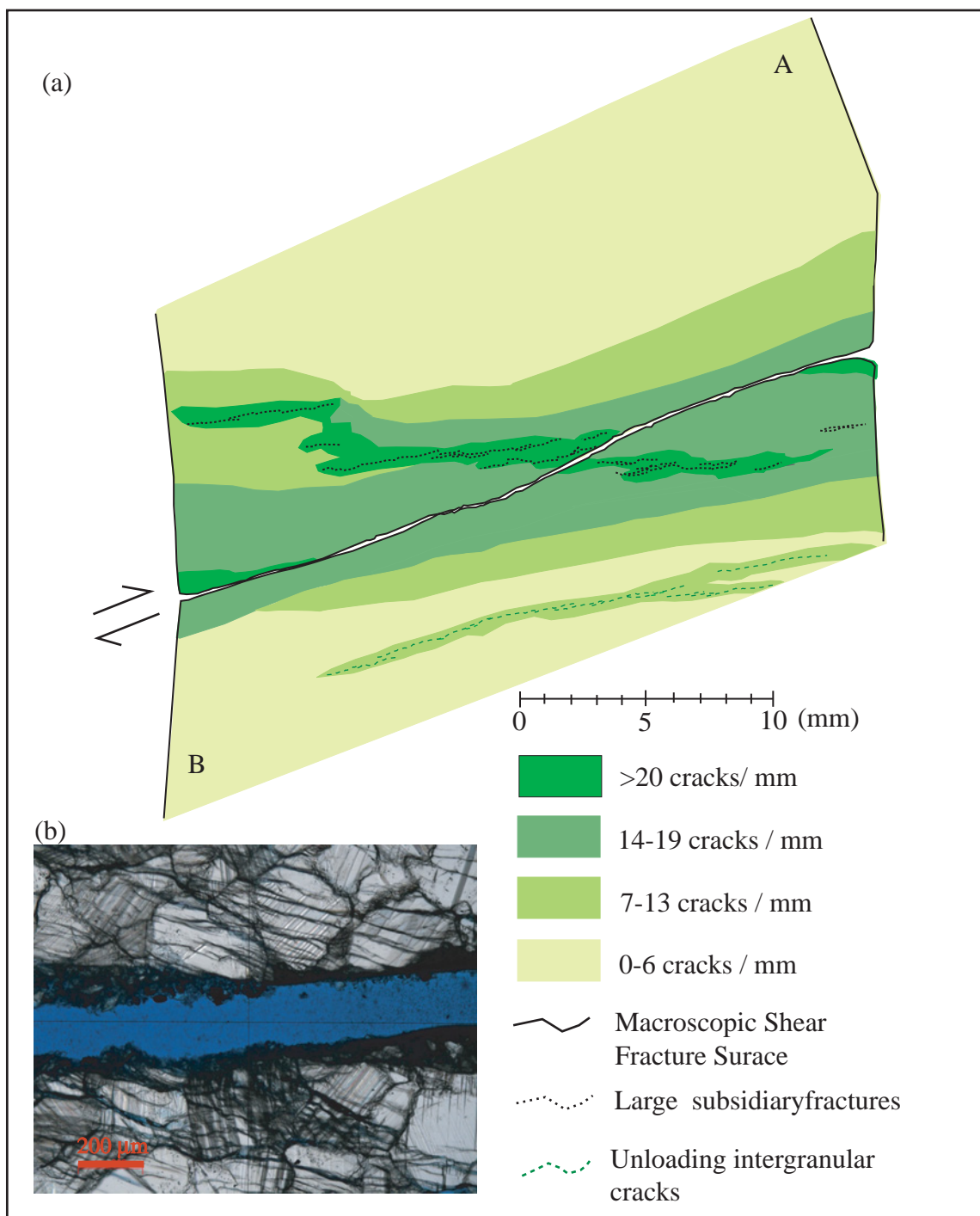
Figure 16. Microfracture density map of a shear fracture (#4693, 170MPa). Microfracture density shaded map. (b) Photograph taken in the central region of the fracture surface that displays the microfracture preferred orientation as well as the deformation along the surface (see text for further description).

(a)

A

B

1cm

(c)

290

A

280

Large Subsidiary Fracture

Macroscopic Fracture Surface

B

Deg. from vertical axis

270

260

250

Unloading Fracture

240

-6   -4   -2   0   2   4   6

Distance from the macroscopic fracture surface (mm)

(b)
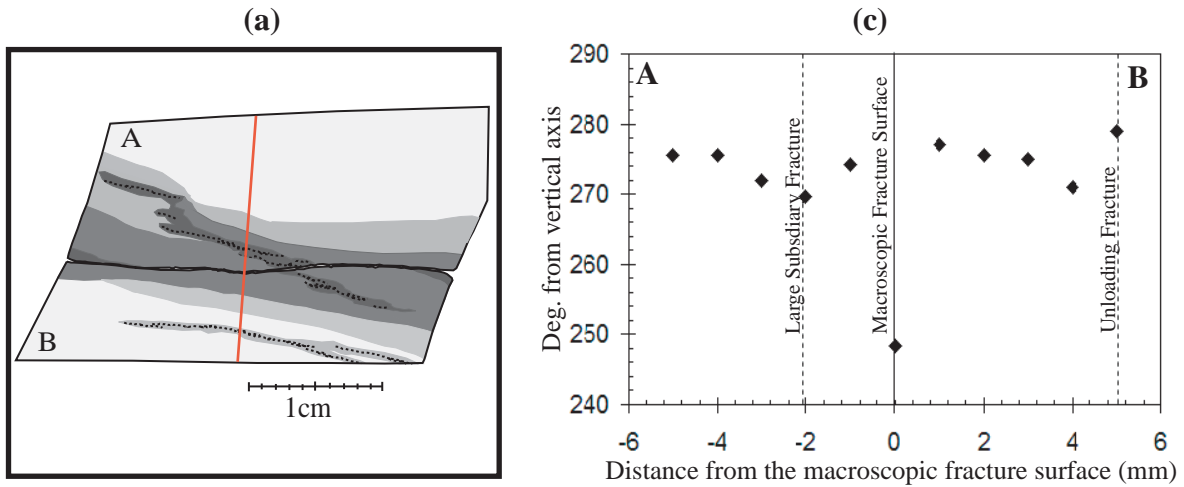
D*	1 mm	2 mm	3 mm	4 mm	5 mm	Total
side A						
side B						
trend** (deg)	A: 274.3 B: 277.1	A: 269.7 B: 275.6	A: 272.2 B: 275.0	A: 275.6 B: 271.0	A: 275.6 B: 279.0	A: 273.5 B: 275.7

*Distance from the fault
**Mean microfracture orientation w/rt vertical core axis

Figure 17. Shear microfracture orientations (#4693,170 MPa). This sample has a macroscopic fracture angle of 21.6^o from the horizontal axis of the core. (a) Schematic microfracture density shaded map, red line is the location of the traverse along which the microfracture orientations were measured. The microfractures were measured with respect to the vertical core axis (b) Rose diagrams show distribution of microfracture orientations with distnce from the macroscopic fracture surface. Data are grouped in 1 mm bins. The trends listed are the mean orientation of microfractures. (c) The mean microfracture orientations with respect to the vertical axis are plotted as a function of distance from the macroscopic fracture surface.

from the macroscopic hybrid fracture surface and are referred to as pinnate fractures [*Engelder*, 1989].

The pinnate microfractures are oriented parallel to σ_1 and nearly all can be correlated with pinnate fractures on the other side of the macroscopic fracture surface (Fig. 18 & Fig. 19). This ability to correlate the pinnate fractures across the hybrid fracture surface suggests that the pinnate fractures formed before the macroscopic fracture surface. They have a fairly systematic spacing and similar lengths (Table 2). In general, the average length of the pinnate fractures and their spacing decreases as a function of confining pressure.

The compressive hybrid (120 MPa) contains intergranular microfractures that are about 5 to 7 grains in length and are generally oriented parallel to σ_1 (Fig.19). These microfractures are constrained in a deformation zone that is about 5mm from the macroscopic fracture surface and in the central region of the core. Outside this deformation zone, there are sporadic, cleavage microfractures that are one to two grains in length; they are random in location and orientation. Even though, the density of these sporadic microfractures is similar to that found in the starting material; their lengths tend to be greater.

Similar to the shear fracture sample, the tensional hybrid sample has open fractures that extend from one edge of the sample to the central part of the fracture surface on either side of the macroscopic fracture surface (Fig. 18). These fractures are oriented nearly parallel to σ_1, are similar in morphology to the extension fractures, and they are likely a result of unloading. Additionally, both tensional and compressional

hybrids have intergranular fractures that extend from the edge of the sample into the core (Fig. 18 & Fig. 19); they are most likely associated with experimental edge effects. The density of this type of fractures is higher in the sample deformed at the higher confining pressure. In general, their aperture increases towards the outer edge of the sample.
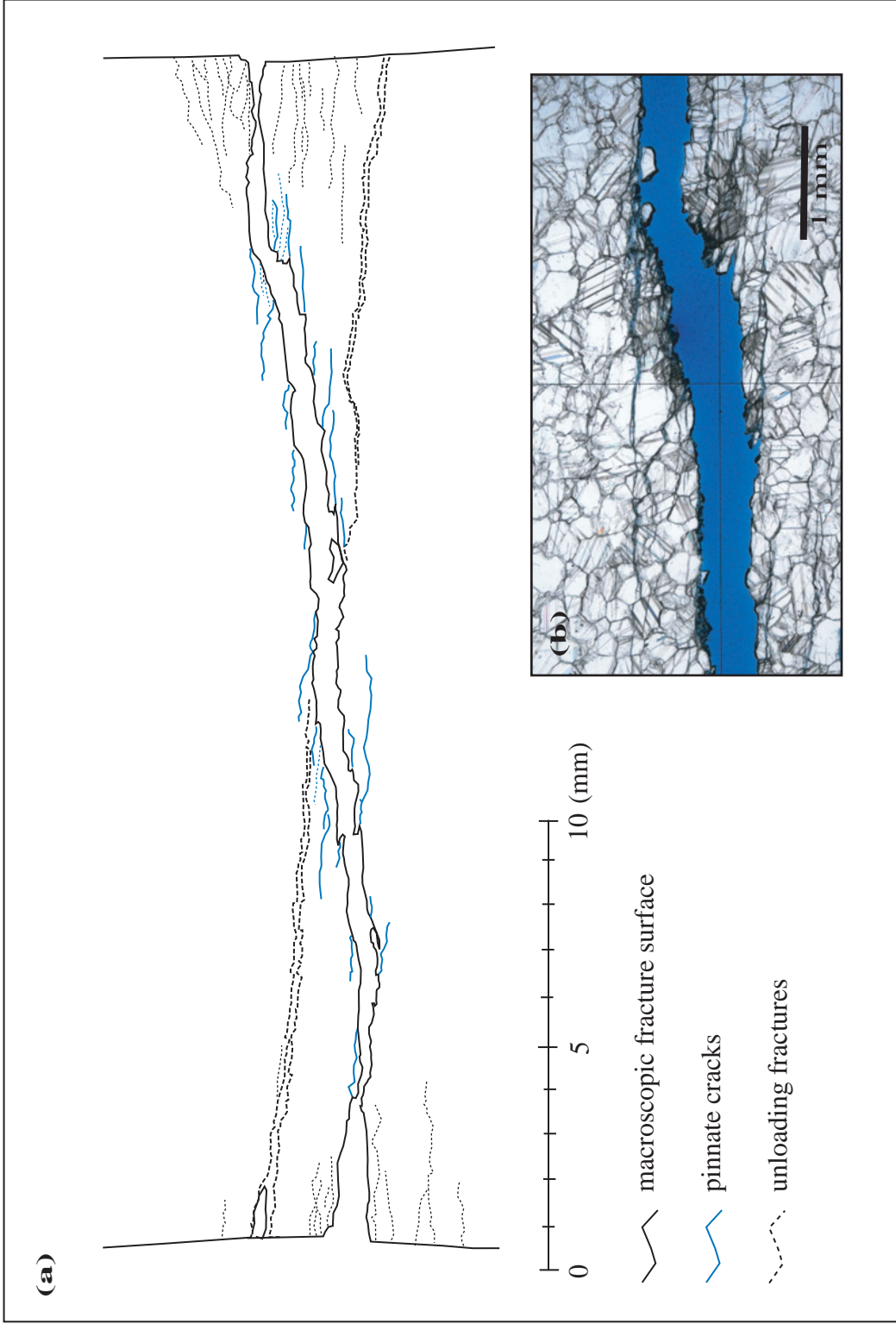
Figure 18. Microfracture map of tensile-hybrid fracture (#4709, 90 MPa). Micrograph displays variations of twinning and microfracturing along fracture surface
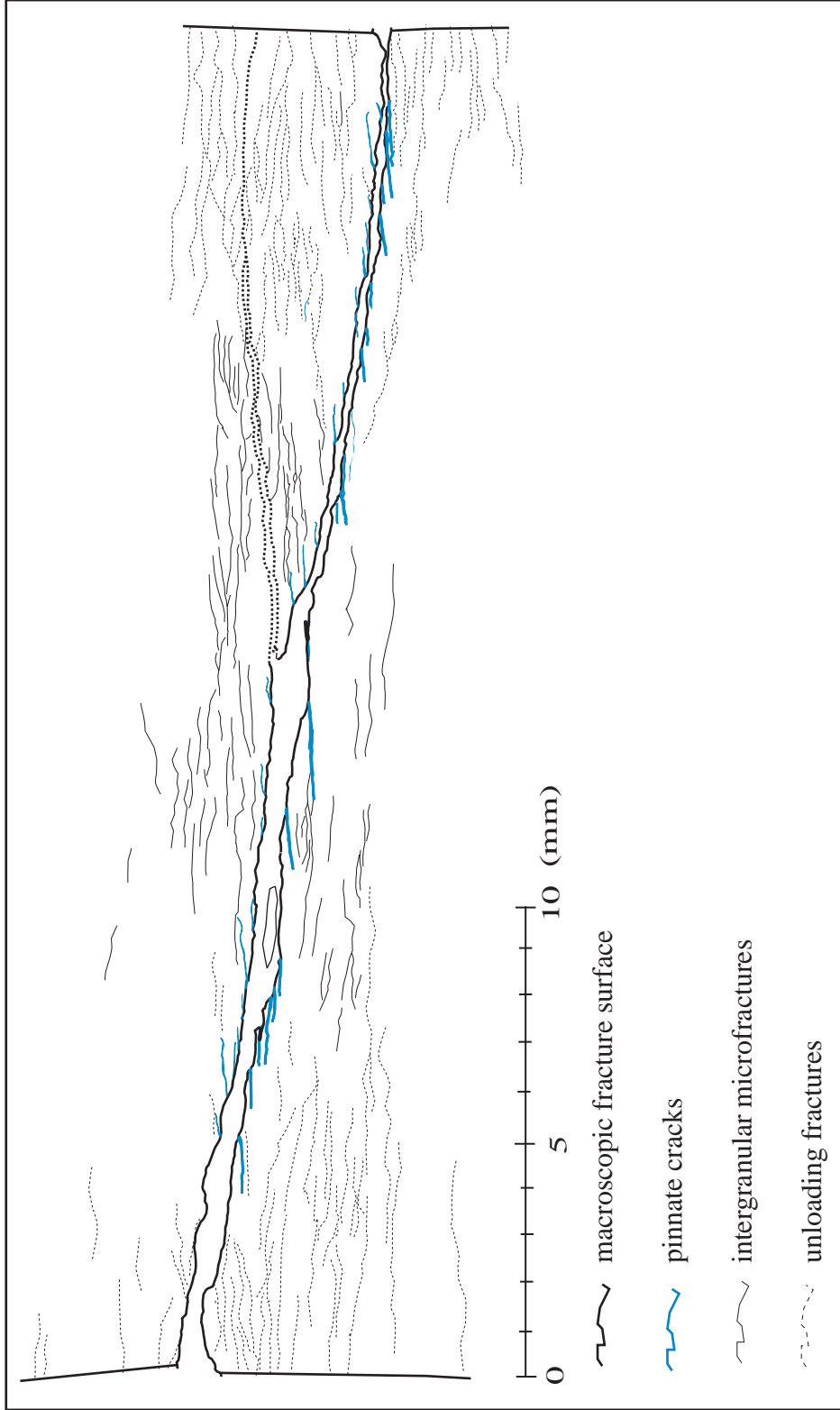
Figure 19. Microfracture map of compresive–hybrid fracture (#4706, 120 MPa).

macroscopic fracture surface

pinnate cracks

intergranular microfractures

unloading fractures

0   5   10 (mm)

Table 2. Spacing to length ratio of pinnate microfractures

P$_c$ (MPa)	Fracture Angle	Spacing (mm)	Length (mm)	S/L
90	6.1°	.294	3.958	.074
100	7.3°	.151	2.092	.072
120	12.4°	.155	1.286	.121

4. DISCUSSION

4.1 Power Spectral Density Analysis

Spectral analysis is used to acquire a statistical description of surface roughness, as a function of scale, from the profiles measured from each deformed sample across the transition from extension to shear fracture.   The power spectral density (PSD) is determined for 12 fracture surfaces. The PSD is calculated for the three central profiles of each fracture surface, which are then averaged at each wavelength, and then subjected to a low-pass filtering using an averaging window of 10 data points. The results are presented in log-log plots of PSD versus wavelength, λ (Fig. 20-22), where λ is the inverse of the spatial frequency, f.   Lines of constant amplitude versus wavelength ($\gamma=A/\lambda$) are shown in the plots to facilitate the analysis of the scale dependence of roughness [*Power and Tullis*, 1991].

PSD functions, G (f), that are linear in the log-log plots can be described with a power law of the form

$$G\ (f) = Cf^{-\alpha} \tag{1}$$

or as

$$\log G\ (f) = \log C - \alpha \log\ (f) \tag{2}$$

to illustrate linearity, where α and C are constants that describe the surface roughness. A surface with a PSD that is fit by equation (1) is said to be fractal in character. A surface best described by a self-similar fractal model will display a statistically similar character at any magnification as the entire profile of the macroscopic surface. A surface best described with a self-affine fractal model is one for which a portion of the

Figure 20. Power spectral density plots of extension fracture profiles. PSD is plotted as a function of wavelength (λ) for extension fractures in the direction (a) parallel and (b) perpendicular to maximum dip. Dotted lines are contours of amplitude to wavelength ratio (γ)

Figure 21. Power spectral density plots of shear fracture profiles. PSD is plotted as a function of wavelength (λ) for shear fractures in the direction (a) parallel and (b) perpendicular to slip. Dotted lines are contours of amplitude to wavelength ratio (γ)
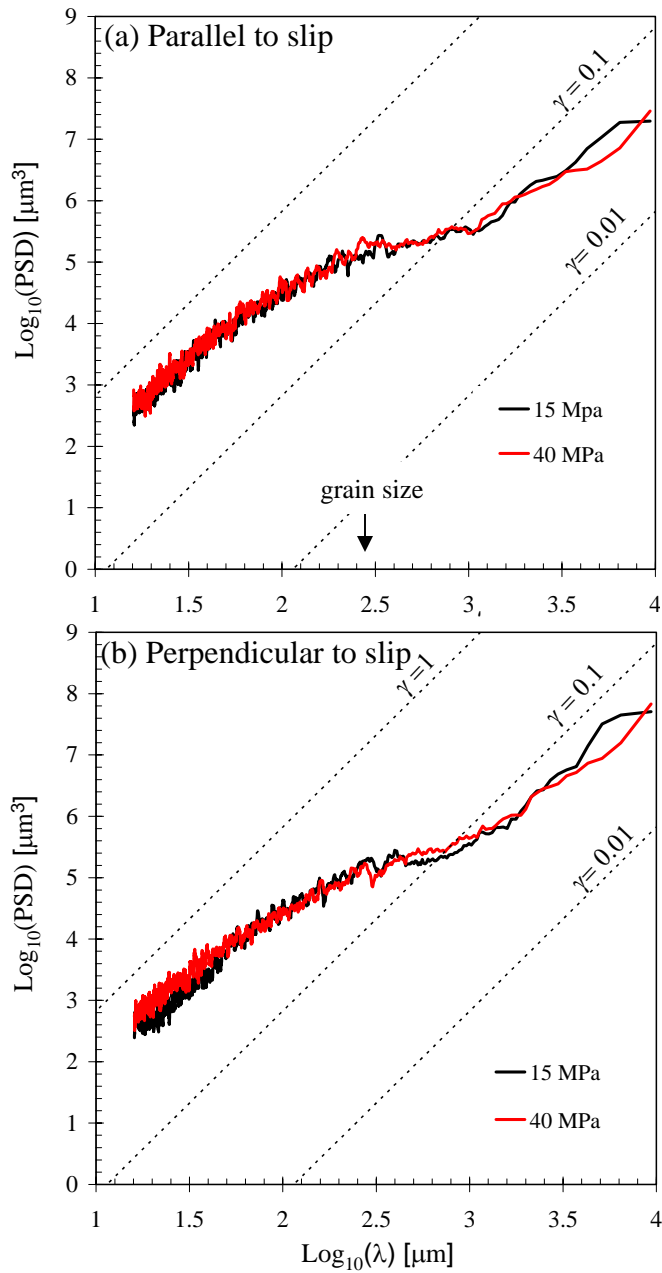
Figure 22. Power spectral density plots of hybrid fracture profiles. PSD is plotted as a function of wavelength (λ) for hybrid fractures in the direction (a) parallel and (b) perpendicular to slip. Dotted lines are contours of amplitude to wavelength ratio (γ)

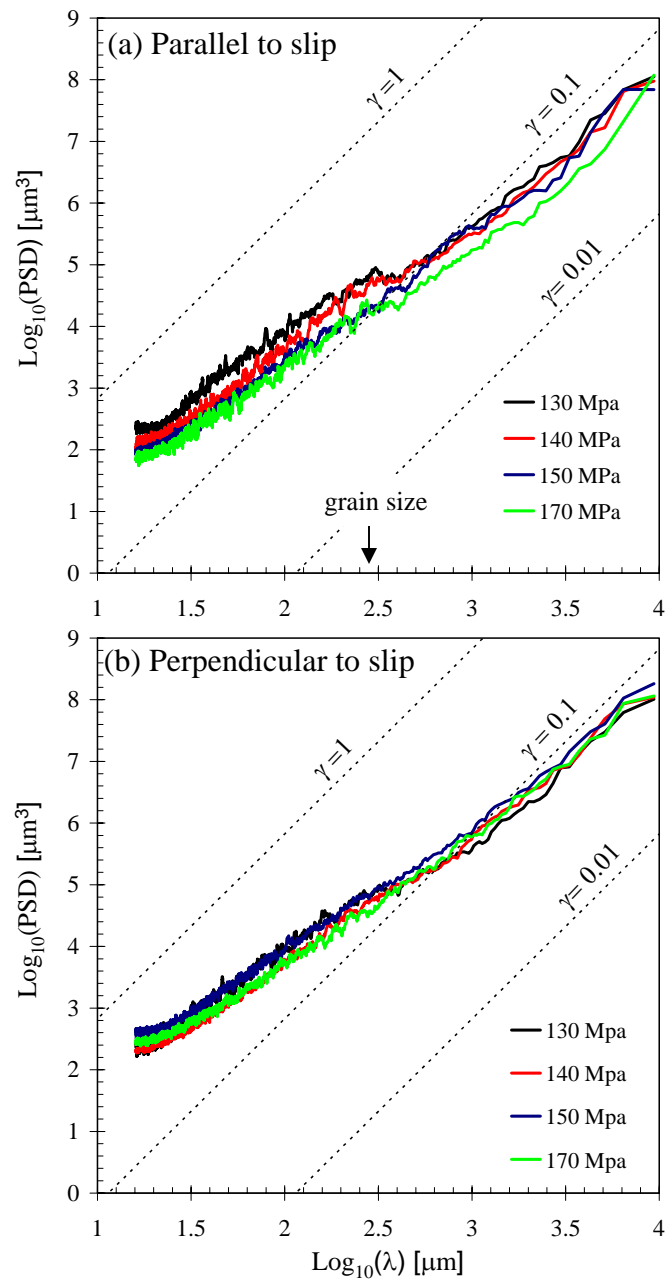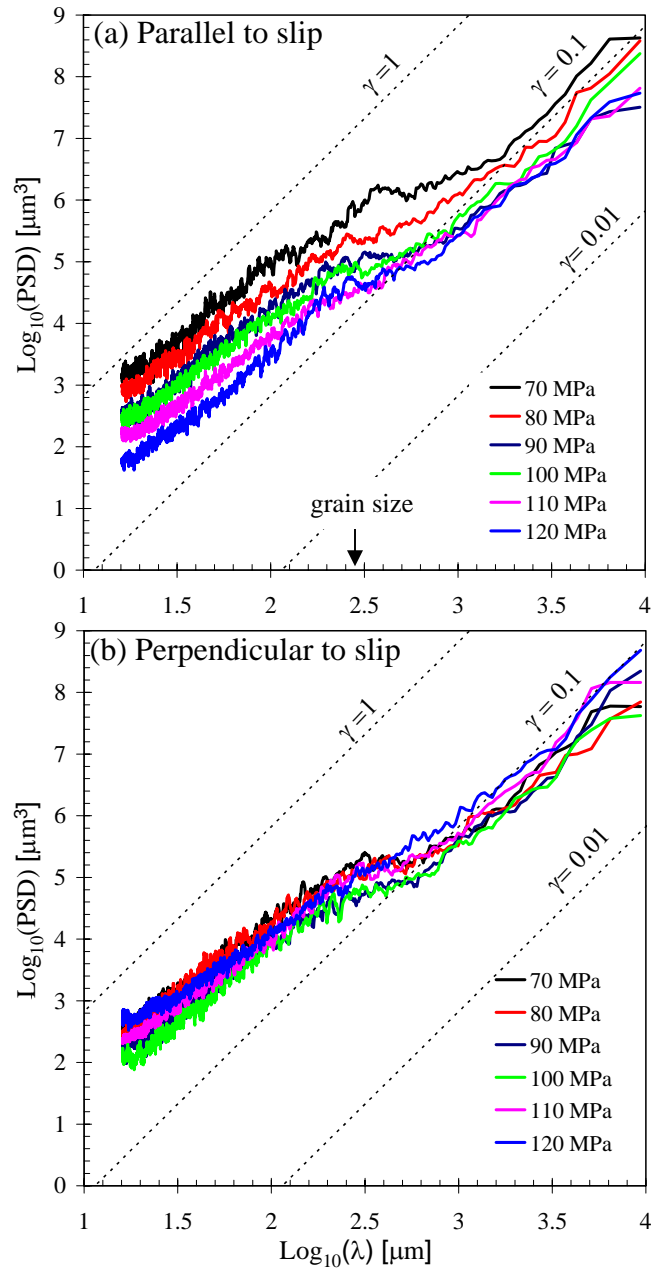profile is statistically similar to the entire profile only if different magnifications are used

perpendicular and parallel to the surface [*Mandebrot*, 1983]. The parameter α is the

slope of the power spectrum that describes how the surface roughness changes with scale.

In a self-similar surface $\alpha=3$. Log_{10} (C) describes the steepness of the surface

topography, which is related to γ, at $\lambda=1$ [*Brown and Scholz*, 1985; *Power and Tullis*,

1991; *Power et al.*, 1987]. As a result, rougher surfaces will tend to have larger intercept

values than smoother surfaces.

The relative roughness of the different fracture types is determined by least

square fitting of (z) to all PSD curves and plotting log_{10} (C) as a function of confining

pressure (Fig. 23). Overall, surface roughness is greatest in the extension fracture regime.

In the direction parallel to slip, the roughness decreases linearly with confining stress

through the hybrid and shear fracture regimes. In the direction perpendicular to slip, the

roughness is fairly constant through out the hybrid regime, and increases somewhat in

the shear regime. In these orientations, profiles cross slip-parallel grooves and striations

that are characteristic of shear fracture and that contributes to the large scale roughness.

Overall, the PSD throughout the entire wavelength spectrum, both parallel and

perpendicular to slip, are self-affine because $\alpha < 3$. Accordingly, the surfaces are

generally rougher at the microscale and smoother at the macroscale. This can be seen by

comparing the PSD curves to lines of constant roughness, γ. PSD for wavelengths

(λ) less than one millimeter plot above the $\gamma = 0.1$ contour, and for wavelengths greater

than one millimeter plot below the $\gamma = 0.1$ contour (Fig. 20-22). With increasing

confining pressure, variations in roughness between the small and large scales decrease,

as a result shear fractures have a more uniform and smoother roughness along the entire wavelength spectrum; that is they are the closest to self-similar surfaces.

Although the PSD of all fracture surfaces are similar, there are systematic variations across the transition from extension to shear fracture. All of the PSD curves are fairly linear except for a marked reduction in slope at a length scale that is approximately equivalent to the host rock grain size and the magnitude of the shear displacement (Fig. 20-22). The reduced slope occurs over a wavelength interval that decreases with an increase in confining pressure to the point that the slope break is completely absent in the PSD for the shear fracture formed at the highest confining pressure (Fig. 24).

Because the PSD curves display a distinct slope change over intermediate wavelengths on the order of the grain size, we investigate scale dependence of roughness by determining the best fit of (z) to the curves at the wavelengths that are less than the grain size and greater than the grain size (Fig. 25). In general, the slope of the best fit lines increases with confining pressure for wavelengths less than the grain size, and decrease with confining pressure for wavelengths greater than the grain size.

Large scale features of the fracture surfaces generally decrease in magnitude from extension-to-shear except at the transition from extension to tensile hybrid fracture (Fig. 26). PSD curves display a marked increase in power for tensile hybrids deformed at 70 and 80 MPa (Fig. 22) in the larger wavelength spectrum. The increase in power is controlled by the formation of fracture surfaces that leads to a higher roughness in the direction of slip. With increasing pressure the power of the PSD for large wavelengths
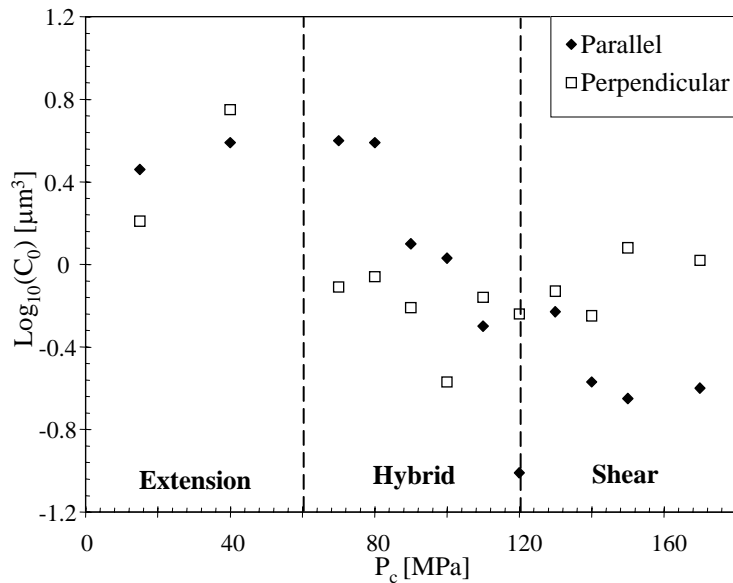
Figure 23. Plot of $\log_{10}(C)$ vs. confining pressure.
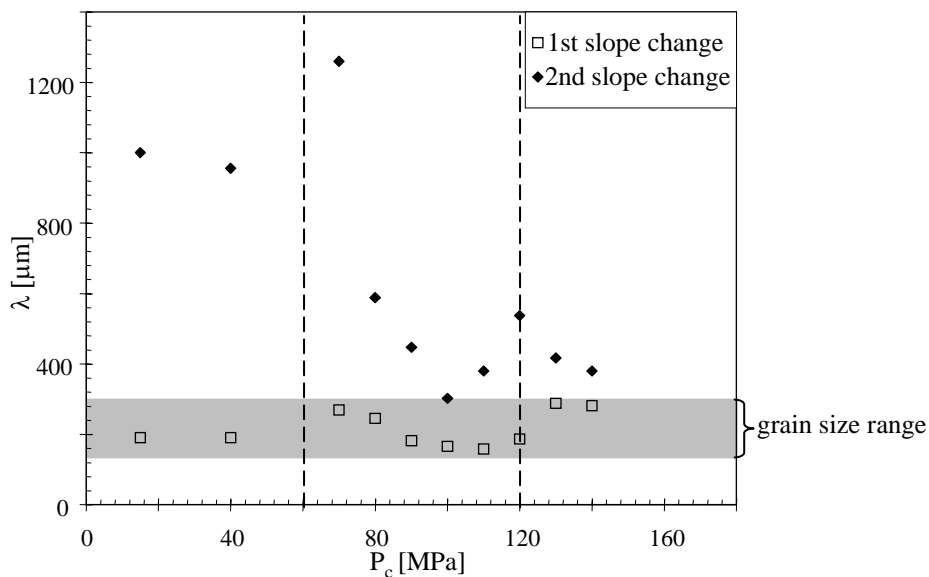
Figure 24. Plot of alpha (α) vs. confining pressure. Wavelengths at which first and second slope changes occur in PSD curve as a function of confining stress (P_c) in the direction parallel to slip.
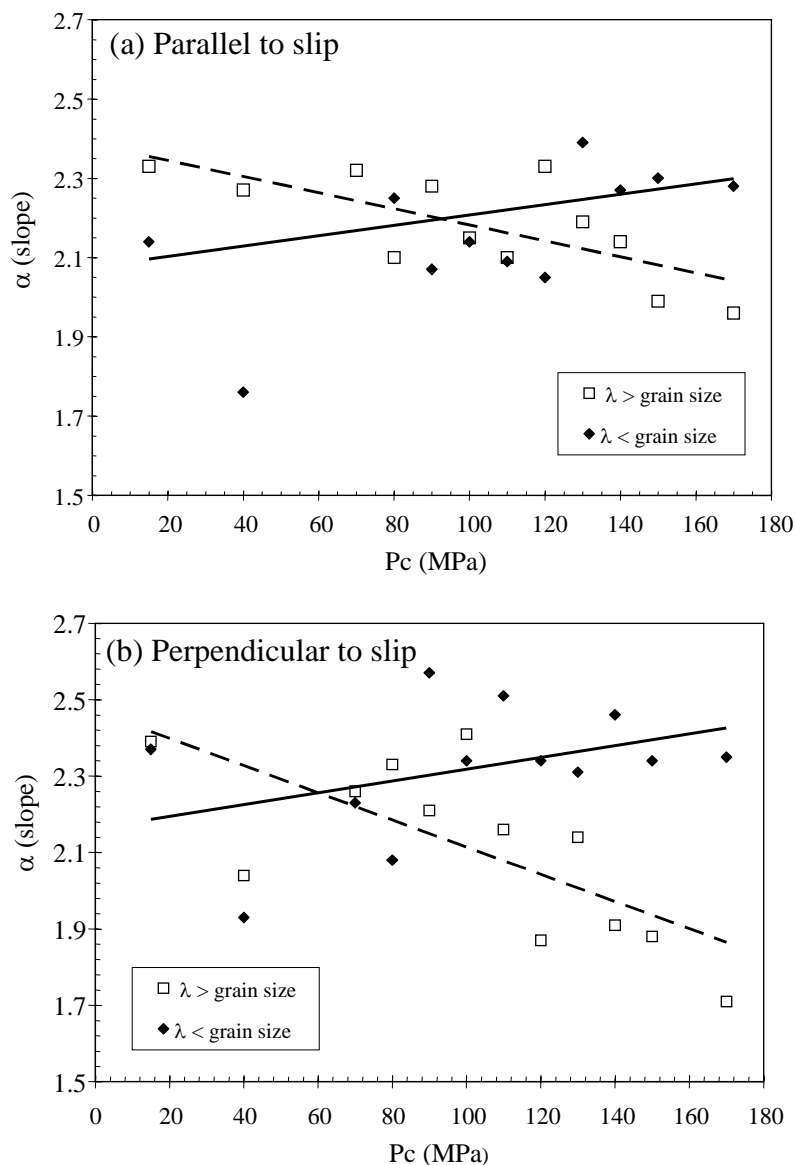
Figure 25. Plot of alpha (α) vs. confining pressure at different scales. Variations of slope (α) of PSD curves above and below the grain size range in the directions parallel (a) and perpendicular (b) to slip or maximum dip. The solid line is the best fit line for wavelengths below the grain size, the dashed line is the best fit line for wavelengths above the grain size range.
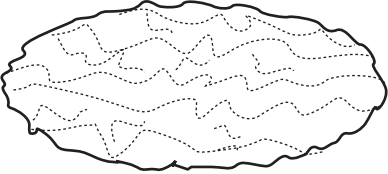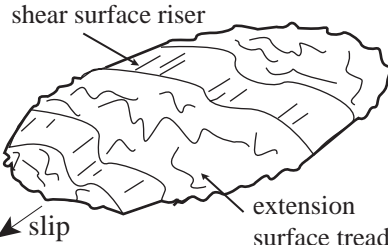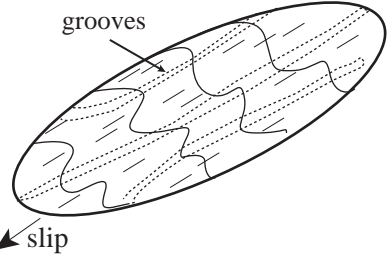
Fracture Type	Surface Schematic	Large Scale Roughness Features
Extension		Irregular roughness that does not have a fabric in any orientation
Hybrid	shear surface riser / slip / extension surface tread	Steps are made up of rough extension surface treads and smoother shear surface risers
Shear	grooves / slip	Rough in the direction perpendicuar to slip due to development of grooves

Figure 26. Schematic diagrams and descriptions of large scale roughness features of the fracture transition.

decreases systematically in the hybrid and shear fracture regimes which correlates with smaller spacing of steps with pressure. PSD curves of shear fractures (Fig.21) in the direction perpendicular to slip plot closer to the $\gamma = 1$ contour than the compressive hybrid fractures (Fig.22). This shows that at wavelengths above 1mm, in the direction perpendicular to slip, shear fractures are slightly rougher than compressive hybrid fractures.

At the lower confining pressures, the microscale roughness of fractures in marble is dictated by the cleavage of calcite. As seen in the SEM images of the extension fracture surface, cleavage steps, river patterns and discontinuities at grain boundaries lead to high power for small wavelength roughness (Fig. 8). Once the grain size scale is exceeded, intergranular cracking follows grain boundary surfaces, cleavage surfaces and abrupt steps or changes in surface orientation are less pronounced. At greater confining pressures the microscale roughness is not only dictated by the cleavage and grain boundaries, but also is influenced by competing mechanisms. With increasing confining pressure the features characteristic of cleavage that are exposed on the surfaces decrease in density. This decrease could be attributed processes such as: wear during slip, slower rupturing speeds at high confining pressures, and crystal plastic processes such as, twinning and dislocation glide. To investigate the effects of wear, profiles were made of fracture surfaces before and after the removal of the loose comminuted material on the macroscopic fracture surfaces by gentle cleaning. Profiles of the cleaned surfaces for compressive hybrid and shear fracture surfaces, display rougher characters at the scale
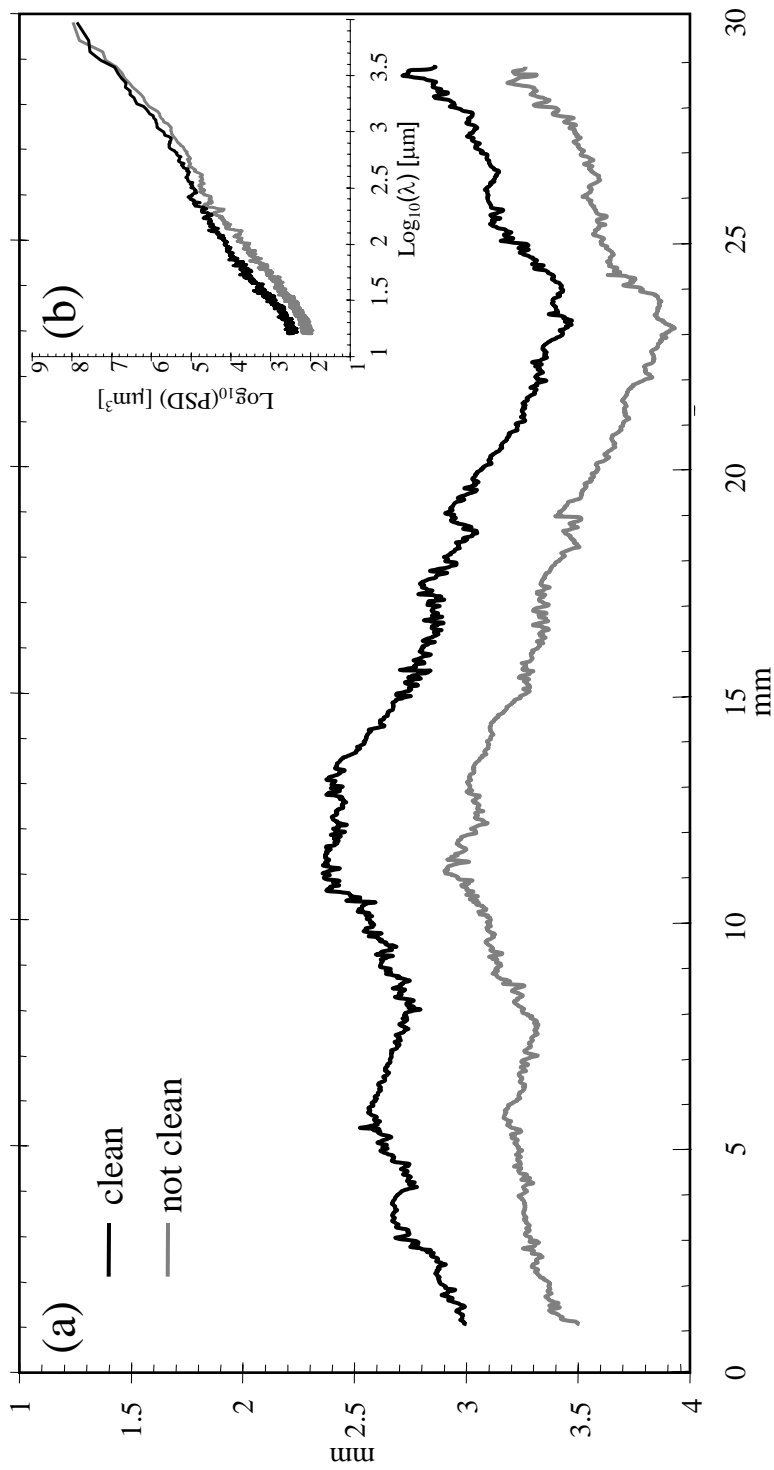
Figure 27. Shear Fracture (#4705, 140 MPa) before and after cleaning. (a) profiles of surface before and after comminuted material was washed off. (b) PSD curves of each profile show that after cleaning the surface is rougher.

below the grain size (Fig. 27). Interestingly, the slope of the PSD curve of the clean

fracture surface remains very similar to that of the same surface before cleaning.

4.2 Roughness of Natural Fractures

The variations in roughness of the fracture surfaces produced in the laboratory

across the transition from extension to shear fracture are similar to the roughness

reported for natural joints and faults [*Brown and Scholz*, 1985; *Power and Tullis*, 1991;

Power et al., 1988]. Like joints, the experimentally produced extension fractures have

isotropic roughness (i.e., they have similar roughness in all orientations). Similar to

natural faults, the experimentally produced shear fractures are characterized by

anisotropic roughness, where the roughness is greater in the direction perpendicular to

slip and lower in the direction parallel to slip. In addition, the laboratory extension

fractures and tensile hybrid fractures have PSD values that are similar to those reported

for joints, especially at the lower wavelengths [Fig. 28 & Fig. 29; *Brown and Scholz*,

1985]. Compressive hybrids and shear fractures produced in the laboratory are smoother

than joints but significantly rougher than faults found in nature, especially at the

wavelengths smaller than one millimeter (Fig. 30). The smoother character of faults

relative to the shear fractures produced in the lab can not be attributed to weathering,

since weathering tends to increase roughness in natural fault surfaces [*Mayer et al.*, 2000;

Wallace, 1984]. Studies of fault surfaces in limestone have found that older fault scarps

display more pitting resulting from dissolution weathering than younger fault scarps

[*Wallace*, 1984]. Dissolution of smooth cleavage planes increases the roughness
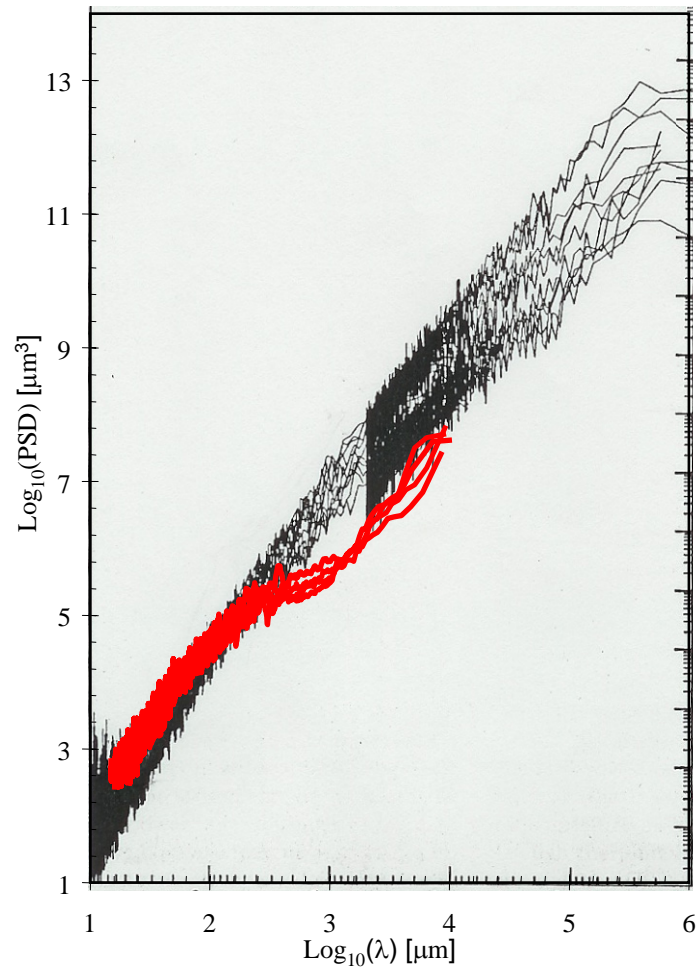
Figure 28. PSD plots of natural joints and extension fractures. Black curves are data from natural joints and bedding planes. Red curves are data from extension fractures in the directions parallel and perpendicular to maximum dip in Carrara marble samples, there is a very good correlation of these curves, especially at the wavelengths smaller than 1mm. [A modification from *Brown and Scholtz*, 1987].
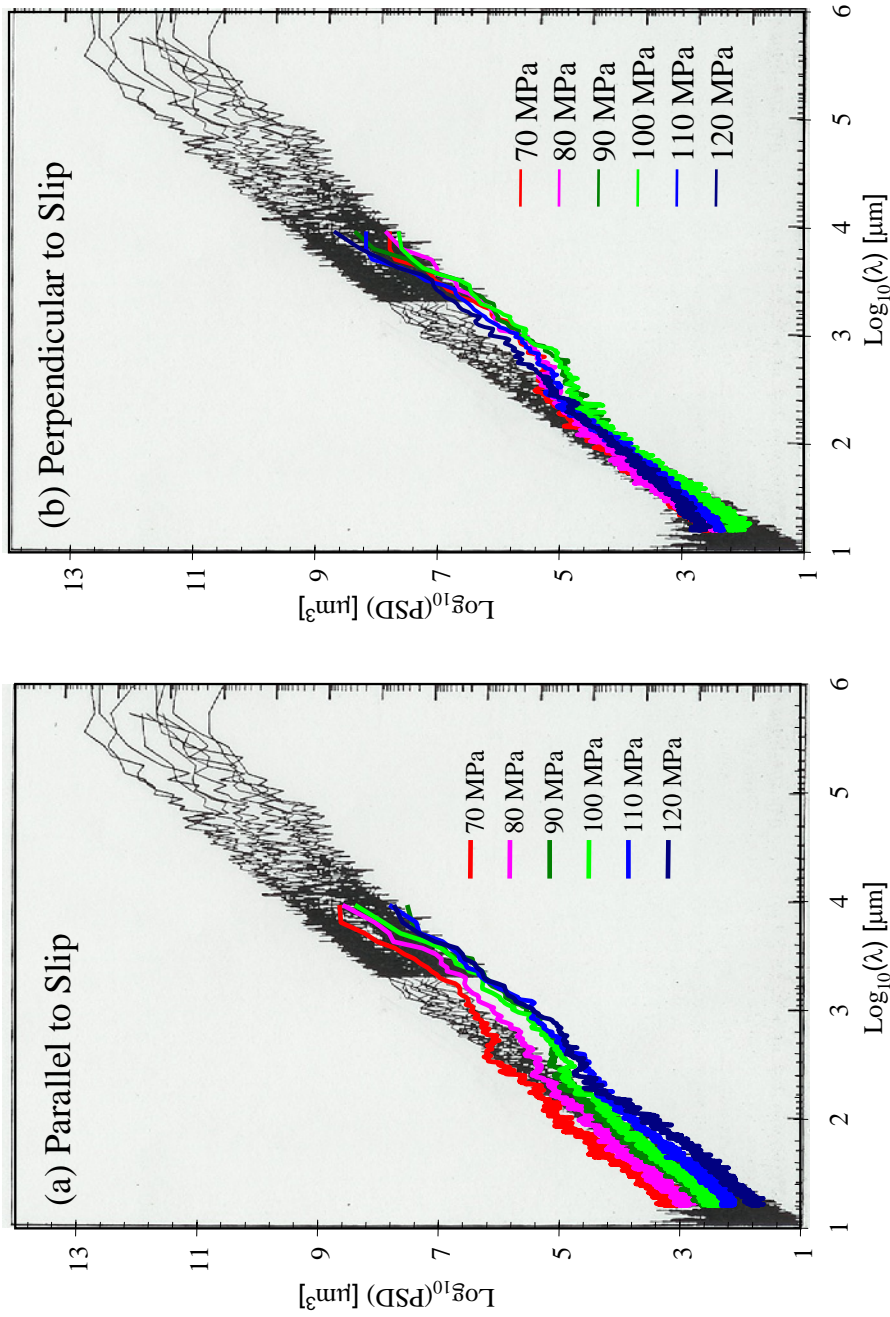
Figure 29. PSD plots of natural joints and hybrid fractures. Black curves are data from natural joints and bedding planes. Colored curves are data from hybrid fractures in the directions parallel and perpendicular to maximum slip in Carrara marble samples, there is a very good correlation between the natural fractures and the experimental hybrids across the entire wavelength spectrum. [A modification from *Brown and Scholz*, 1987]
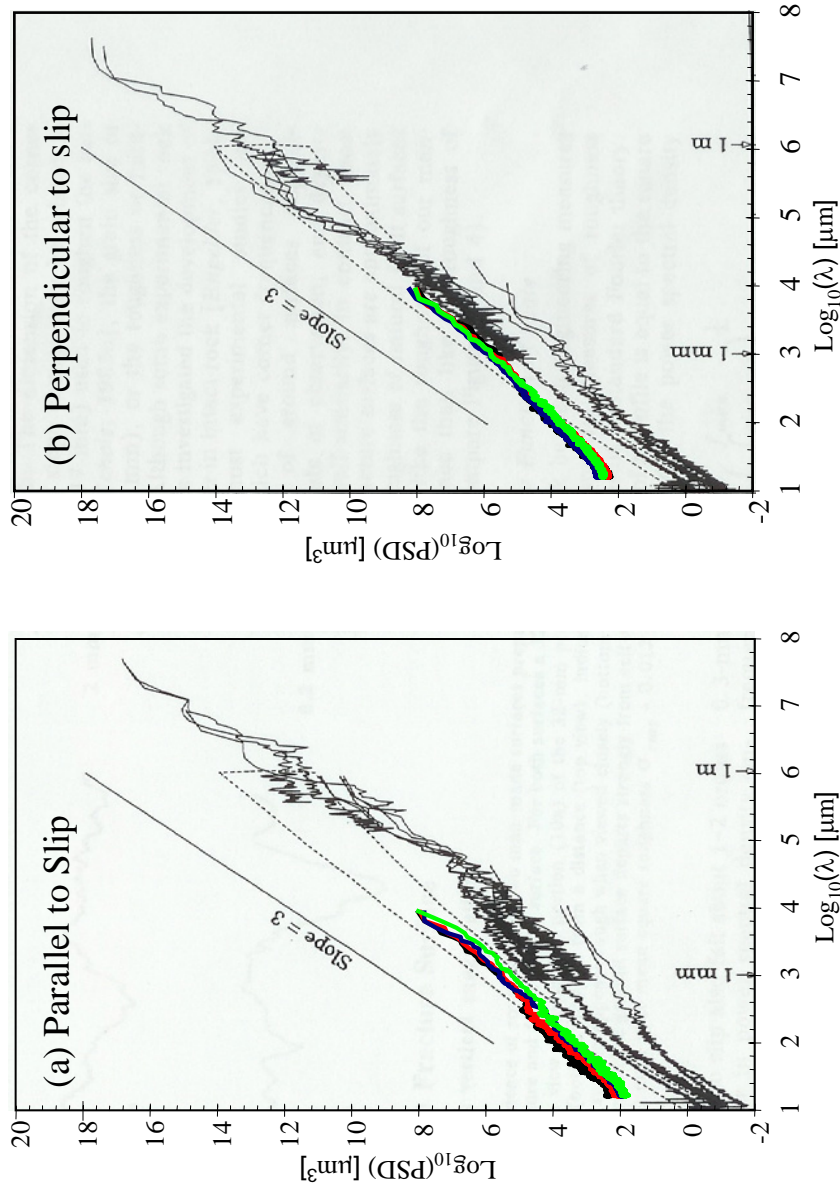
Figure 30. PSD plots of natural faults and shear fractures. Black lines are PSD curves for natural faults in the direction (a) parallel and (b) perpendicular to slip. Colored curves are data for experimental shear fractures in the direction parallel and perpendicular to slip. Experimental fractures are rougher at scales below 1mm with respect to natural fractures. [A modification from *Power and Tullis, 1998*]

and fractal character at scales smaller than the grain size [*Mayer et al.*, 2000].

Wear models are often based on the premise that the roughness of self-similar natural faults increases with the amount of shear displacement [*Power et al.*, 1988]. Slip produces mismatches between the two opposing fault surfaces. The mismatch between the surfaces grows gradually with slip as larger asperities are juxtaposed resulting in greater roughness as a function of slip. However, this model does not address how roughness would change at the scales less than the grain size, where the roughness tends to be self-affine. Increasing roughness as a function of slip, over the wavelength spectrum as a whole, would not necessarily increase roughness at scales less than the grain size.

4.3 Triaxial Extension vs. Triaxial Compression

In triaxial extension experiments of Carrara Marble the macroscopic fracture angles produced are smaller by at least 15° relative to those resulting from triaxial compression at the same maximum and minimum principal stress [*Ramsey*, 2003]. In triaxial extension, the intermediate principal stress, σ_2, is greater than in triaxial compression, which apparently influences the macroscopic fracture orientation [*Mogi*, 1967]. It would be important to consider if this also influences the micromechanisms associated with fracture formation. Microstructural observations from triaxial compression experiments in the brittle regime of Carrara Marble [*Fredrich et al.*, 1989] document that the micromechanisms activated during shear fracture under triaxial extension are similar. In the brittle regime strain partitioning is primarily distributed

between microfracturing and twinning. In some cases twins serve as stress concentrators that nucleate microfractures, however, most microfractures are oriented parallel to the maximum principal stress. The microfractures associated with the shear fracture are between three to four grains in length. *Frederich* [1989] makes qualitative observations that with increasing confining pressure the microfracture length decreases. She suggests that the localization of the macroscopic fracture in the sample is not only associated with microfracture density (spacing) but also with microfracture length, since both of these factors are important to microfracture interaction in the process zone.

4.4 The Step-crack Model

At the initial stages of loading, shear fracture development under compressive stress states is interpreted to initiate with random generation of opening mode microfractures [*Reches and Lockner*, 1994]. As loading approaches the fracture strength of the material, microfractures extend from flaws such as grain boundaries. Neighboring, en echelon, tensile microfractures, oriented perpendicular to the least compressive principal stress, interact and facilitate the dilation of one another in a recursive manner. This generates the process zone that forms the through going macroscopic fracture surface. Most models of shear fracture development consider the mechanical interaction of microfractures essential to the formation of a macroscopic fracture surface that ultimately will be inclined to the maximum and minimum principal stress directions. The model by *Reches and Lockner* [1994] predicts that microfractures form in en echelon arrays by interaction with neighboring microfractures, and that the macroscopic

fracture orientation reflects the spacing and length of the en echelon microfractures. *Engelder* [1999] proposes that this stepped-crack model can explain the formation of hybrid fractures with stepped-surface-geometries and fracture orientations that are at low angles to the maximum principal stress direction. Although theory relating the length and spacing of microfractures to stress states is lacking in the *Reches and Lockner* [1994] model, it is expected that the length-to-spacing-ratio may increase with a decrease in compressive stress. Since self-arrest of the opening-mode cracks propagating from starter flaws is favored under compressive stress states, the length of such microfractures should increase with increasing tensile stress. If correct, the stepped-crack geometry, in which the treads and risers form by the linkage of en echelon microfractures, could apply to the hybrid regime, where there is a progressive decrease in step-size across the transition from extension fracture to shear fracture.

As Engelder [1999] proposed, the step-crack model [*Reches and Lockner*, 1994] is consistent with the observations presented in this study of hybrid fracture development :

1. The surface profiles of hybrid fractures have rough treads perpendicular to the minimum principal stress direction that are linked by smoother risers.

2. The en echelon array of treads step in the opposite direction relative to the sense-of-shear; this geometry would be inconsistent with the simple linkage of pre-existing fractures [*Segall and Pollard*, 1983].

3. In thin section, en echelon pinnate microfractures with systematic spacing can be correlated from one side of the macroscopic fracture to the other.

4. The space to length ratio of the en-echelon pinnate microfractures increases as a function of increasing confining pressure and is similar to the relationship proposed by *Reches and Lockner* [1994].

5. CONCLUSIONS

1. Like natural fractures, extension fractures have isotropic roughness and shear fractures have anisotropic roughness. Laser profilometry of fracture surfaces show that microscopic roughness decreases gradually across the extension-to-shear fracture transition both parallel and perpendicular to slip direction. In general, the macroscopic roughness decreases across the transition in the direction parallel to slip, though there is an exception to this at the boundary between extension fractures and tensile-hybrid fractures. The development of steps in the tensile hybrids results in higher roughness for this fracture type than the extension fractures which formed at lower confining stresses, in the direction parallel to slip. In the direction perpendicular to slip, macroscopic roughness is relatively constant across the extension-to-shear fracture transition; however, the development of grooves in shear fractures slightly increases roughness for this orientation. Overall, experimental fracture surfaces are self-affine since they are rougher at the microscale than at the macroscale.

2. The hybrid fractures in this experimental suite follow the geometrical characteristics proposed in the step-crack model [*Engelder*, 1989; *Reches and Lockner*, 1994]. In general, they have a stepped macroscopic fracture surface. The treads of the steps have characteristics of extension fracture surfaces and the risers have characteristics of shear fracture surfaces. The treads have a right-stepping left lateral geometry with compressional bends where shear occurs.

3. Hybrid fractures have pinnate fractures that emanate from the macroscopic fracture surface. The pinnate fractures can be correlated from one side of the macroscopic fracture surface to the other suggesting that they are precursory to the macroscopic fracture surface. They are generally systematically spaced and their lengths are similar across the same surface. The lengths and the spacing of the pinnate fractures decrease as a function of confining pressure. The spacing to length ratio of the pinnate fractures and the macroscopic orientation of the fracture surface are consistent with the step-crack model of fault formation [*Reches and Lockner*, 1994]

REFERENCES

Bendat, J.S., and A.G. Piersol, *Random Data: Analysis and Measurement Procedures*, 407 pp., John Wiley & Sons, Inc., New York, 1971.

Brace, W.F., Brittle fracture of rocks, in *State of Stress in the Earth's Crust*, edited by W.R. Judd, pp. 111-180, Elsevier, New York, 1964.

Brown, S.R., and C.H. Scholz, Broad bandwidth study of the topography of natural rock surfaces, *Journal of Geophysical Research*, *90* (B14), 12575-12582, 1985.

Engelder, T., The analysis of pinnate joints in the Mount Desert Island Granite: implications for post-intrusion kinematics in the coastal volcanic belt, Maine, *Geology*, *17*, 564-567, 1989.

Engelder, T., Transitional-tensile fracture propagation: a status report, *Journal of Structural Geology*, *21*, 1049-1055, 1999.

Fredrich, J.T., B. Evans, and T.-F. Wong, Micromechanics of the brittle to plastic transition in Carrara marble, *Journal of Geophysical Research*, *94* (B4), 4129-4145, 1989.

Friedel, J., *Dislocations*, 320-347 pp., Pergamon Press, New York, 1964.

Groshong, R.H., Strain calculated from twinning in calcite, *Geological Society of America Bulletin*, *83*, 2025-2048, 1972.

Hancock, P.L., Brittle microtectonics: principles and practice, *Journal of Structural Geology*, *7* (3/4), 437-457, 1985.

Hull, D., *Fractography Observing, Measuring and Interpreting Fracture Surface Topography*, 125-137 pp., Cambridge University Press, Cambridge, 1999.

Jaeger, J.C., and N.G.W. Cook, *Fundamentals of Rock Mechanics*, 187-195 pp., Chapman and Hall, London, 1969.

Mandebrot, B.B., *The Fractal Geometry of Nature*, 468 pp., W. H. Freman, New York, 1983.

Mardon, D., A.K. Kronenberg, J. Handin, M. Friedman, and J.E. Russell, Mechanisms of fracture propagation in experimentally extended Sioux quartzite, *Tectonophysics*, *182*, 259 -278, 1990.

Mayer, L., J. Rakovan, and E. Rufe, Microtopographic evolution of mineral surfaces as tools to identify and date young fault scarps in bedrock, *Journal of Geodynamics*, *29*, 393-406, 2000.

Mogi, K., Effect of the intermediate principal stress on rock failure, *Journal of Geophysical Research*, *72* (20), 5117-5131, 1967.

Pieri, M., L. Burlini, K. Kunze, I. Stretton, and D.L. Olgaard, Rheological and microstructural evolution of Carrara marble with high shear strain: results from high temperature torsion experiments, *Journal of Structural Geology*, *23*, 1393-1413, 2001.

Power, W.L., and T.E. Tullis, Euclidean and fractal models for description of rock surface roughness, *Journal of Geophysical Research*, *96* (B1), 415-424, 1991.

Power, W.L., T.E. Tullis, S.R. Brown, G.N. Boitnott, and C.H. Scholz, Roughness of natural fault surfaces, *Geophysical Research Letters*, *14* (1), 29-32, 1987.

Power, W.L., T.E. Tullis, and J.D. Weeks, Roughness and wear during brittle faulting, *Journal of Geophysical Research*, *93* (B12), 15,268-15,278, 1988.

Ramsey, J.M., Experimental Study of the transition from brittle shear fractures to joints, M.S. thesis, Texas A&M University, College Station, 2003.

Ramsey, J.M., and F.M. Chester, Hybrid fractures and the transition from extension fracture to shear fracture, *Nature*, *428*, 63-66, 2004.

Reches, Z., and D.A. Lockner, Nucleation and growth of faults in brittle rock, *Journal of Geophysical Research*, *99* (B9), 18159-18173, 1994.

Segall, P., and D.D. Pollard, Nucleation and growth of strike slip faults in granite, *Journal of Geophysical Research*, *88* (B1), 555-568, 1983.

Wallace, R.E., Faulting related to the 1915 earthquakes in Pleasant Valley, Nevada, *U.S. Geological Survey Professional Paper*, *1274-A*, 34-38, 1984.

VITA

Name: Erika Rodriguez

Address: 7366 Timber Creek, San Antonio, TX 78227

Email Address: erodriguez@geo.tamu.edu

Education: B.S., Geology, New Mexico Institute of Mining and Technology 2001

                    M.S., Geology, Texas A&M University, 2005